

Phase-field modeling of fatigue coupled to cyclic plasticity in an energetic formulation^{☆,☆☆}

Jacinto Ulloa^a, Jef Wambacq^a, Roberto Alessi^b, Geert Degrande^a, Stijn François^a

^a*KU Leuven, Department of Civil Engineering, Kasteelpark Arenberg 40, B-3001 Leuven, Belgium*

^b*Università di Pisa, Department of Civil and Industrial Engineering, Largo Lucio Lazzarino 2, 56122 Pisa, Italy*

Abstract

This paper presents a modeling framework to describe the driving mechanisms of cyclic failure in brittle and ductile materials, including cyclic plasticity and fatigue crack growth. A variational model is devised using the energetic formulation for rate-independent systems, coupling a phase-field description of fatigue fracture to a cyclic plasticity model that includes multi-surface kinematic hardening, gradient-enhanced isotropic hardening/softening and ratcheting. The coupled model embeds two distinctive fatigue effects. The first captures the characteristic features of low-cycle fatigue, driven by the accumulation of plastic strains, while the second accounts for high-cycle fatigue, driven by free energy accumulation. The interplay between these mechanisms allows to describe a wide range of cyclic responses under both force loading and displacement loading, as shown in several numerical simulations. Moreover, the phase-field approach to fracture accounts for the initiation and propagation of fatigue-induced cracks.

Keywords: Fatigue fracture, Cyclic plasticity, Ratcheting, Damage/phase-field models, Energetic/variational formulation, Gradient-extended internal variables

1. Introduction

Solids and structures subjected to cyclic loading exhibit a progressive reduction in load-carrying capacity due to material degradation. This phenomenon is important in several branches of engineering, accounting for (up to) 90% of all structural failures [1]. Despite its importance, the study of cyclic failure, including cyclic plasticity and various fatigue regimes, remains an open issue in computational mechanics. The objective of this study is to propose a model to describe cyclic failure in brittle and ductile materials using a mathematically and physically sound variational framework, and to demonstrate its capabilities in benchmark numerical simulations.

[☆] *Postprint version.*

^{☆☆} *Published version:* J. Ulloa, J. Wambacq, R. Alessi, G. Degrande, and S. François. Phase-field modeling of fatigue coupled to cyclic plasticity in an energetic formulation. *Computer Methods in Applied Mechanics and Engineering*, 373:113473, 2021. DOI: <https://doi.org/10.1016/j.cma.2020.113473>

*Corresponding author: Jacinto Ulloa

Email addresses: jacintoisrael.ulloa@kuleuven.be (Jacinto Ulloa), jef.wambacq@kuleuven.be (Jef Wambacq), roberto.alessi@unipi.it (Roberto Alessi), geert.degrande@kuleuven.be (Geert Degrande), stijn.francois@kuleuven.be (Stijn François)

Depending on the loading conditions and material properties, different fatigue regimes can be distinguished [2]. At load amplitudes above a certain threshold, yet small enough to avoid plastic strains, high-cycle fatigue occurs, governed by a slow material degradation that leads to brittle fractures. Under higher load amplitudes, low-cycle fatigue occurs. This phenomenon is driven by a combination of damage and plastic strains, where the initial cyclic response can be rather complex. In particular, cyclic hardening or cyclic softening effects are generally observed, as well as asymmetrical loading effects, such as ratcheting under force loading and stress relaxation under displacement loading [3–6]. These cyclically plastic responses may occur in a transient fashion, leading to stabilized hysteresis loops. The interplay between these phenomena and material degradation strongly influences material behavior in the low-cycle fatigue regime.

Classical fatigue analyses are based on (semi-) empirical methods, which require extensive data from experimental tests. Fatigue life is commonly assessed using Wöhler curves, relating the applied stress amplitude to the number of cycles to failure in constant-amplitude cyclic loading. Statistical approaches such as the Basquin relation [7] fit empirical equations to Wöhler curves. The drawback of these techniques lies in their empirical nature, requiring tuning of problem-dependent parameters that do not account for the underlying fracture process. Concerning fatigue fracture analysis, the conventional approach is based on Paris’ law [8] and its extensions [9, 10], which relate crack growth rate to stress intensity factors. Paris’ law is rooted in classical fracture mechanics and is therefore unable to describe crack initiation and the final rupture stage. An alternative approach to fatigue consists of introducing fatigue effects in constitutive material models [11], providing a more versatile framework [12]. However, most models include parameters with no clear physical interpretation, and often use Paris-type laws and Wöhler curves as input data [13].

This study adopts the framework of constitutive models with non-local internal variables. To properly describe failure modes, such as brittle and quasi-brittle fractures, or shear bands in ductile materials, a suitable representation of highly localized strains is required. Strain localization is captured by models with softening behavior, which, however, render the mathematical problem ill-posed and result in pathological mesh-dependence in numerical simulations. To alleviate these issues, regularization can be introduced by means of non-local effects that are governed by internal length scales. Gradient-enhanced models, as outlined in the formulations of Maugin [14] and Miehe [15], are common examples of this approach.

In relation to gradient-enhanced models, developments in the modeling of crack nucleation and propagation have taken place in the last two decades due to the variational approach to fracture [16–18]. This framework links classical fracture mechanics to gradient-damage models. Specifically, the Γ -converging regularization of Bourdin et al. [17] towards the Griffith-based energy functional of Francfort and Marigo [16] can be alternatively viewed as a phase-field description of fracture [19–21] or as a gradient-damage model [22–25]. This framework is able to naturally predict crack initiation and propagation in complex crack topologies, overcoming limitations of classical fracture mechanics and discrete-crack approaches, such as XFEM-based methods [26–28]. While initially developed for brittle fracture, several extended phase-field models have been developed in the literature, some of which are outlined in Wu et al. [29].

Two extensions of the phase-field approach to fracture are particularly relevant for the purposes of this work. The first is the extension to plasticity [30–41], which allows to describe the nucleation and propagation of ductile cracks. The second is the extension to fatigue that has gained attention in the recent literature [12, 13, 42–48]. This approach to fatigue has been shown to consistently recover experimental observations such as Wöhler curves and Paris’ law. Nevertheless, extensions of phase-field-based fatigue to account for the main features of low-cycle fatigue are still missing in the literature. A suitable representation of low-cycle fatigue must include cyclic plasticity, for which most theories [5, 49–52] can be linked to the Armstrong–Frederick model [53, 54]. It is the objective of the present work to address this topic.

The governing equations of a large class of material models can be derived from the theory of generalized standard materials [55–58]. In this setting, the evolution problem follows from an internal energy density and a dissipation potential, ensuring an a priori fulfilment of the second law of thermodynamics. This theory can be reformulated in a variational setting, where the governing equations emerge as the Euler-Lagrange equations of an energy minimization principle that can be solved using numerical optimization techniques. Pioneering works on this topic focused on rate-type variational principles for local elastoplasticity [59–65], and have been extended to, e.g., gradient-enhanced models [15, 66–68]. In these works, the principle of virtual power is generally used to derive the governing equations [15, 69, 70].

The energetic formulation [71, 72] is a particularly attractive variational framework that furnishes a unified and rigorous mathematical setting for rate-independent dissipative processes. The theory handles non-smooth evolutions (discontinuities in space and time), since no derivatives appear in the most general setting, and provides tools for the analysis of structural and material stability [73]. Some applications of the energetic formulation in the modeling of dissipative solids include plasticity [74, 75], (quasi-)brittle [18, 22, 24, 76] and ductile [31, 37, 38, 77] fracture, shape-memory alloys [78, 79] and fatigue [12, 13].

An important limitation of the theory of generalized standard materials and its variational formulation is the restriction imposed by the principle of maximum dissipation. This condition implies the normality law for the evolution equations and thus, in principle, excludes non-associative models. Nevertheless, extensions to non-associativity can be made by considering certain state-dependent dissipation potentials. References in this line of work include [76, 80–83]. These developments are essential from a practical standpoint because a variational structure is no longer restricted to associative models, accounting for more realistic representations of, for instance, plasticity in geomaterials and in metals under cyclic loading.

In the framework of the energetic formulation, we propose a model that couples the phase-field approach to fatigue, as suggested by Alessi et al. [12] and Carrara et al. [13], to the main mechanisms of cyclic plasticity. The proposed model includes multi-surface kinematic hardening and a non-associative ratcheting variable [52], as well as gradient-enhanced isotropic hardening/softening, governed by its own characteristic length scale. The coupling of the phase-field-based fatigue model to cyclic plasticity renders a general framework that encompasses the characteristic behavior of both high- and low-cycle fatigue in a thermodynamically consistent setting and is able to objectively represent fatigue crack growth with plasticity. Several examples

are presented to highlight the versatility of the proposed framework to capture representative responses under both force loading and displacement loading.

This paper is organized as follows. To establish the modeling framework, section 2 presents the energetic formulation applied to a general class of dissipative solids with gradient-enhanced internal variables. These concepts are then used to construct the fatigue model with cyclic plasticity in section 3, with numerical experiments presented in section 4.

We employ the following notations. A dot (\cdot) and a colon ($:$) denote inner products with simple and double contraction, respectively. The Euclidean norm of \square is denoted as $\|\square\|$. The notation $\square_{\text{dev}} := \square - (1/3) \text{tr} \square \mathbf{1}$ is used to denote the deviatoric part of a tensor \square . The notation $\|\bullet\|_{\square} := \sqrt{\bullet : \square : \bullet}$ for a second-order tensor \bullet is used, where \square is a fourth-order tensor. Functions and function values are denoted using the same symbol: \square is a space-time-dependent function evaluated as $\square(\mathbf{x}, t)$. Time-dependent functions evaluated at a point in space are denoted with a vector argument, e.g. $\square(\mathbf{x})$, while space-dependent functions parametrized by time are denoted with a scalar argument, e.g. $\square(t)$. These distinctions are made when required for clarity purposes, and are otherwise omitted and inferred from context. The time derivative is denoted as $\dot{\square}$, while the spatial gradient reads $\nabla \square$. In the context of convex analysis, $\partial \square$ is the multivalued subdifferential with respect to \square , while $\partial \square(\bullet)$ is the subdifferential of \square at \bullet . Finally, $\delta_{\square} := \partial \square - \text{div}[\partial_{\nabla \square}]$ is the spatial Euler-Lagrange derivative with respect to \square .

2. Variational framework

2.1. Problem outline

Consider an arbitrary solid of mass density ρ occupying a domain $\Omega \subset \mathbb{R}^d$ of dimension $d \in \{1, 2, 3\}$, with boundary $\Gamma \subset \mathbb{R}^d$. The boundary consists of a Dirichlet part Γ_{D} with imposed displacements $\bar{\mathbf{u}}(\mathbf{x}, t) \in \mathbb{R}^d$ and a Neumann part Γ_{N} with imposed tractions $\bar{\mathbf{t}}(\mathbf{x}, t) \in \mathbb{R}^d$, such that $\Gamma_{\text{D}} \cup \Gamma_{\text{N}} = \Gamma$ and $\Gamma_{\text{D}} \cap \Gamma_{\text{N}} = \emptyset$. The solid may be subjected to volume forces per unit mass, denoted as $\mathbf{b}(\mathbf{x}, t) \in \mathbb{R}^d$.

The deformation process is assumed to be quasi-static, occurring in a pseudo-time (loading) interval $\mathbb{T} := [0, t_{\text{max}}]$. The displacement field is given by

$$\mathbf{u}: \begin{cases} \Omega \times \mathbb{T} \rightarrow \mathbb{R}^d, \\ (\mathbf{x}, t) \mapsto \mathbf{u}(\mathbf{x}, t), \end{cases}$$

which is kinematically admissible, satisfying boundary conditions on Γ_{D} . Assuming the small-strain hypothesis, the compatible strain tensor $\boldsymbol{\varepsilon}(\mathbf{x}, t) \in \mathbb{R}_{\text{sym}}^{d \times d} := \{\mathbf{e} \in \mathbb{R}^{d \times d} \mid \mathbf{e} = \mathbf{e}^{\text{T}}\}$ is obtained from

$$\boldsymbol{\varepsilon} := \nabla^{\text{s}} \mathbf{u}, \quad \text{with} \quad \nabla^{\text{s}} \square := \frac{1}{2} (\nabla \otimes \square + \square \otimes \nabla).$$

The Cauchy stress tensor $\boldsymbol{\sigma}(\mathbf{x}, t) \in \mathbb{R}_{\text{sym}}^{d \times d}$ is statically admissible, satisfying equilibrium for all $t \in \mathbb{T}$:

$$\text{div} \boldsymbol{\sigma} + \rho \mathbf{b} = \mathbf{0} \quad \text{in} \quad \Omega \quad \text{and} \quad \boldsymbol{\sigma} \cdot \mathbf{n} = \bar{\mathbf{t}} \quad \text{on} \quad \Gamma_{\text{N}}, \quad \text{with} \quad \mathbf{u} = \bar{\mathbf{u}} \quad \text{on} \quad \Gamma_{\text{D}}. \quad (1)$$

The dissipative mechanisms that lead to inelastic material behavior are characterized by a generic set of internal variables and their spatial gradients:

$$\mathbf{a}: \begin{cases} \Omega \times \mathbb{T} \rightarrow \mathbb{R}^m, \\ (\mathbf{x}, t) \mapsto \mathbf{a}(\mathbf{x}, t), \end{cases} \quad \nabla \mathbf{a}: \begin{cases} \Omega \times \mathbb{T} \rightarrow \mathbb{R}^{md}, \\ (\mathbf{x}, t) \mapsto \nabla \mathbf{a}(\mathbf{x}, t). \end{cases}$$

We denote the set of primary fields by $\mathbf{q} := \{\mathbf{u}, \mathbf{a}\}$ and the constitutive state by $\mathbf{c} := \{\boldsymbol{\varepsilon}, \mathbf{a}, \nabla \mathbf{a}\}$. Here, \mathbf{a} is a vector arrangement of m components associated to both scalar- and tensor-valued internal variables.

2.2. Generalized standard materials

Let $\psi := \psi(\boldsymbol{\varepsilon}, \mathbf{a}, \nabla \mathbf{a})$ denote a Helmholtz-type internal energy density. To ensure physical soundness, the second law of thermodynamics is taken as an a priori restriction, given, for isothermal processes, by the Clausius-Planck inequality

$$\boldsymbol{\sigma} : \dot{\boldsymbol{\varepsilon}} - \dot{\psi}(\boldsymbol{\varepsilon}, \mathbf{a}, \nabla \mathbf{a}) \geq 0. \quad (2)$$

The constitutive stress-strain relation

$$\boldsymbol{\sigma} = \frac{\partial \psi}{\partial \boldsymbol{\varepsilon}}(\boldsymbol{\varepsilon}, \mathbf{a}, \nabla \mathbf{a}) \quad (3)$$

directly follows from equation (2), along with the dissipation rate inequality

$$\phi = \mathbf{s} \cdot \dot{\mathbf{a}} \geq 0, \quad \text{with} \quad \mathbf{s} = -\delta_{\mathbf{a}} \psi(\boldsymbol{\varepsilon}, \mathbf{a}, \nabla \mathbf{a}). \quad (4)$$

The set \mathbf{s} contains the thermodynamic forces, or generalized stresses, conjugate to \mathbf{a} .

A thermodynamically admissible dissipation potential is defined as $\phi := \phi(\dot{\mathbf{a}}, \nabla \dot{\mathbf{a}}; \mathbf{c}) \geq 0$, which is assumed to be convex with respect to $\{\dot{\mathbf{a}}, \nabla \dot{\mathbf{a}}\}$ and to vanish for null rates. The dependence of the dissipation potential on the state \mathbf{c} is a generality that accounts for a wide class of material models [57]. The dissipation potential may also depend on history variables, not included in \mathbf{c} but derived from its time history [12, 84], as well as on the generalized stresses \mathbf{s} , as for the case of non-associative models [76, 83, 85]. These more general cases will emerge in the model proposed in section 3. For notational simplicity and without losing generality, only dependence on \mathbf{c} is considered in the abstract formulation presented in this section. For rate-independent processes, ϕ is a homogeneous function of first degree in $\{\dot{\mathbf{a}}, \nabla \dot{\mathbf{a}}\}$, such that

$$\phi(b\dot{\mathbf{a}}, b\nabla \dot{\mathbf{a}}; \mathbf{c}) = b\phi(\dot{\mathbf{a}}, \nabla \dot{\mathbf{a}}; \mathbf{c}), \quad \forall b \geq 0.$$

As a consequence, ϕ is not differentiable at null rates, and, from equation (4), it follows that

$$\mathbf{s} \in \partial_{\dot{\mathbf{a}}} \phi(\dot{\mathbf{a}}, \nabla \dot{\mathbf{a}}; \mathbf{c}) - \text{div} [\partial_{\nabla \dot{\mathbf{a}}} \phi(\dot{\mathbf{a}}, \nabla \dot{\mathbf{a}}; \mathbf{c})].$$

The evolution equation of \mathbf{a} then takes the form

$$\delta_{\mathbf{a}} \psi(\boldsymbol{\varepsilon}, \mathbf{a}, \nabla \mathbf{a}) + \delta_{\dot{\mathbf{a}}} \phi(\dot{\mathbf{a}}, \nabla \dot{\mathbf{a}}; \mathbf{c}) \ni \mathbf{0}, \quad (5)$$

which is often referred to as Biot's equation (cf. [86]). Equations (1) and (5) represent the strong form of the evolution problem of a general dissipative material model with gradient-enhanced internal variables.

2.3. Energetic formulation

In this section, the governing equations of the evolution problem are recovered in a variational setting. To this end, the basic energy quantities are first introduced in global form. Then, the evolution problem is defined in terms of the energetic formulation for rate-independent systems [72], based on notions of energy balance and stability. These principles naturally lead to an incremental energy minimization problem and constitute the building blocks of the variational fatigue model presented in section 3.

2.3.1. Energy quantities

To characterize how the system stores and dissipates energy in exchange with the external environment, the energetic formulation begins with the definition of global energy functionals. To this end, we denote a general function space of internal variables by \mathcal{A} and the corresponding space of admissible variations that embeds evolution constraints (e.g., irreversibility conditions) by $\tilde{\mathcal{A}}$. The specific form of these function spaces depends on the material model, as will be clear in section 3. The space of kinematically admissible displacement fields and the corresponding space of admissible variations are given by

$$\mathcal{U}(t) := \{\mathbf{w} \in \mathcal{F} \mid \mathbf{w} = \bar{\mathbf{u}}(t) \text{ on } \Gamma_D\} \quad \text{and} \quad \tilde{\mathcal{U}} := \{\tilde{\mathbf{w}} \in \mathcal{F} \mid \tilde{\mathbf{w}} = \mathbf{0} \text{ on } \Gamma_D\}, \quad (6)$$

where the form of \mathcal{F} also depends on the model and is specified in section 3. The space of primary fields then reads $\mathcal{Q} := \mathcal{U} \times \mathcal{A}$, such that $\mathbf{q}(t) \in \mathcal{Q}$ is a process with admissible variations $\tilde{\mathbf{q}} \in \tilde{\mathcal{Q}} := \tilde{\mathcal{U}} \times \tilde{\mathcal{A}}$.

The stored internal energy functional $\mathcal{E}: \mathcal{Q} \rightarrow \mathbb{R} \cup \{+\infty\}$ is given by the state function

$$\mathcal{E}(\mathbf{q}) := \int_{\Omega} \psi(\boldsymbol{\varepsilon}(\mathbf{x}), \mathbf{a}(\mathbf{x}), \nabla \mathbf{a}(\mathbf{x})) \, d\mathbf{x}, \quad (7)$$

while the work of external actions is defined as the time-integral of the external power, namely:

$$\mathcal{L}(\mathbf{u}; [0, t]) := \int_0^t \left[\int_{\Omega} \rho \mathbf{b}(\mathbf{x}, \tau) \cdot \dot{\mathbf{u}}(\mathbf{x}, \tau) \, d\mathbf{x} + \int_{\Gamma_N} \bar{\mathbf{t}}(\mathbf{x}, \tau) \cdot \dot{\mathbf{u}}(\mathbf{x}, \tau) \, dS + \int_{\Gamma_D} \mathbf{t}_r(\mathbf{x}, \tau) \cdot \dot{\mathbf{u}}(\mathbf{x}, \tau) \, dS \right] d\tau, \quad (8)$$

where \mathbf{t}_r is the traction vector on Γ_D . To formulate a stability condition, we introduce the external work distance $\mathcal{T}: \mathbb{T} \times \mathcal{U} \times \mathcal{U} \rightarrow \mathbb{R}$, that is, the work done by the external forces at a given time between two admissible states $\{\mathbf{u}_0, \mathbf{u}_1\}$:

$$\mathcal{T}(t, \mathbf{u}_0, \mathbf{u}_1) = \int_{\Omega} \rho \mathbf{b}(\mathbf{x}, t) \cdot (\mathbf{u}_1(\mathbf{x}) - \mathbf{u}_0(\mathbf{x})) \, d\mathbf{x} + \int_{\Gamma_N} \bar{\mathbf{t}}(\mathbf{x}, t) \cdot (\mathbf{u}_1(\mathbf{x}) - \mathbf{u}_0(\mathbf{x})) \, dS. \quad (9)$$

On the other hand, the dissipative power functional $\mathcal{R}: \tilde{\mathcal{A}} \times \mathcal{Q} \rightarrow [0, +\infty]$ is defined as

$$\mathcal{R}(\dot{\mathbf{a}}; \mathbf{q}) := \int_{\Omega} \phi(\dot{\mathbf{a}}(\mathbf{x}), \nabla \dot{\mathbf{a}}(\mathbf{x}); \mathbf{c}(\mathbf{x})) \, d\mathbf{x}, \quad (10)$$

while the dissipation distance $\mathcal{D}: \mathcal{Q} \times \mathcal{Q} \rightarrow [0, +\infty]$ between two states $\{\mathbf{q}_0, \mathbf{q}_1\}$ reads as follows [71]:

$$\mathcal{D}(\mathbf{q}_0, \mathbf{q}_1) := \inf \left\{ \int_0^1 \mathcal{R}(\dot{\mathbf{a}}(s); \mathbf{q}(s)) \, ds \mid \mathbf{q} \in C^1([0, 1], \mathcal{Q}), \mathbf{q}(0) = \mathbf{q}_0, \mathbf{q}(1) = \mathbf{q}_1 \right\}, \quad (11)$$

with $Q \subset \mathbb{R}^d \times \mathbb{R}^m$. This quantity allows to measure the energy dissipated along arbitrary minimizing paths $\mathbf{q}(s) \in \mathcal{Q}$. For smooth evolutions, the total energy dissipated in $[0, t]$ reads

$$\text{Diss}_{\mathcal{D}}(\mathbf{q}; [0, t]) := \int_0^t \mathcal{R}(\dot{\mathbf{a}}(\tau); \mathbf{q}(\tau)) \, d\tau. \quad (12)$$

For certain dissipation potentials obtained as the time-derivative of an energy function, the dissipated energy is a state function [24, 31]. However, as in the present study, this quantity is generally path-dependent.

2.3.2. Evolution problem

From the basic energy quantities, the evolution problem can be defined in variational form by means of the energetic formulation. This framework is based on a notion of energy balance and either a global or a local stability condition, and is directly related to the incremental energy minimization problem of section 2.4.

Global formulation. A process $\mathbf{q}: T \rightarrow \mathcal{Q}$ is an energetic solution if for all $t \in T$:

$$\mathcal{E}(\mathbf{q}(t)) \leq \mathcal{E}(\tilde{\mathbf{q}}) - \mathcal{T}(t, \mathbf{u}(t), \tilde{\mathbf{u}}) + \mathcal{D}(\mathbf{q}(t), \tilde{\mathbf{q}}), \quad \forall \tilde{\mathbf{q}} = \{\tilde{\mathbf{u}}, \tilde{\mathbf{a}}\} \in \mathcal{Q}, \quad (13)$$

$$\mathcal{E}(\mathbf{q}(t)) + \text{Diss}_{\mathcal{D}}(\mathbf{q}; [0, t]) = \mathcal{E}(\mathbf{q}(0)) + \mathcal{L}(\mathbf{u}; [0, t]). \quad (14)$$

Equations (13) and (14) represent, respectively, the global stability condition and global energy balance, and constitute the most general form of the energetic formulation, with regularity assumptions only required for the external loading functions.

Local formulation. To recover the local governing equations (1) and (5), we depart from the notion of global stability and admit, as candidate solutions, those satisfying a local-directional stability condition. For this purpose, let $h \in \mathbb{R}$ denote a variation parameter and $\tilde{\mathbf{q}} \in \tilde{\mathcal{Q}}$ be test directions in which admissible variations on \mathbf{q} take place. Then, a process $\mathbf{q}: T \rightarrow \mathcal{Q}$ is locally stable if for all $t \in T$, there exists $\bar{h} > 0$ such that

$$\mathcal{E}(\mathbf{q}(t)) \leq \mathcal{E}(\mathbf{q}(t) + h\tilde{\mathbf{q}}) - \mathcal{T}(t, \mathbf{u}(t), \mathbf{u}(t) + h\tilde{\mathbf{u}}) + \mathcal{D}(\mathbf{q}(t), \mathbf{q}(t) + h\tilde{\mathbf{q}}), \quad \forall \tilde{\mathbf{q}} = \{\tilde{\mathbf{u}}, \tilde{\mathbf{a}}\} \in \tilde{\mathcal{Q}}, \quad \forall h \in [0, \bar{h}]. \quad (15)$$

In the context of local stability, it seems reasonable to consider variations in a small neighborhood of the current state, and to restrict the test directions to monotonic radial (straight) paths [78]. In this case, the dissipation distance (11) specializes to

$$\mathcal{D}(\mathbf{q}_0, \mathbf{q}_1) = \left\{ \int_0^1 \mathcal{R}(\dot{\mathbf{a}}(s); \mathbf{q}(s)) \, ds \mid \mathbf{q}(s) = \mathbf{q}_0 + s(\mathbf{q}_1 - \mathbf{q}_0) \right\}. \quad (16)$$

Assuming that the functionals are Gâteaux-differentiable up to a certain order, a differential stability condition can be defined by replacing the right-hand side of the directional stability condition (15) by a Taylor expansion, and enforcing necessary and sufficient conditions of increasing order for inequality (15) to hold true [22, 78]. In this sense, a first-order condition is obtained by the functional derivatives

$$\left. \frac{d}{dh} \mathcal{E}(\mathbf{q} + h\tilde{\mathbf{q}}) \right|_{h=0} - \left. \frac{d}{dh} \mathcal{T}(t, \mathbf{u}, \mathbf{u} + h\tilde{\mathbf{u}}) \right|_{h=0} + \left. \frac{d}{dh} \mathcal{D}(\mathbf{q}, \mathbf{q} + h\tilde{\mathbf{q}}) \right|_{h=0} \geq 0, \quad \forall \tilde{\mathbf{q}} \in \tilde{\mathcal{Q}}. \quad (17)$$

As in equation (17), for notational simplicity, implicit dependence on time (and space) will be omitted hereafter, unless required for clarity purposes. Using the 1-homogeneity of the dissipation potential, we evaluate the Gâteaux derivative of the dissipation distance as

$$\begin{aligned}
\left. \frac{d}{dh} \mathcal{D}(\mathbf{q}, \mathbf{q} + h\tilde{\mathbf{q}}) \right|_{h=0} &= \lim_{h \rightarrow 0} \frac{\mathcal{D}(\mathbf{q}, \mathbf{q} + h\tilde{\mathbf{q}})}{h} \\
&= \lim_{h \rightarrow 0} \frac{1}{h} \int_{\Omega} \left\{ \int_0^1 \phi(\dot{\mathbf{a}}(\mathbf{x}, s), \nabla \dot{\mathbf{a}}(\mathbf{x}, s); \mathbf{c}(\mathbf{x}, s)) ds \mid \mathbf{q}(s) = \mathbf{q} + hs\tilde{\mathbf{q}} \right\} d\mathbf{x} \\
&= \lim_{h \rightarrow 0} \frac{1}{h} \int_{\Omega} \left\{ \int_0^h \phi(\dot{\mathbf{a}}(\mathbf{x}, r), \nabla \dot{\mathbf{a}}(\mathbf{x}, r); \mathbf{c}(\mathbf{x}, r)) dr \mid \mathbf{q}(r) = \mathbf{q} + r\tilde{\mathbf{q}} \right\} d\mathbf{x} \quad (18) \\
&= \lim_{h \rightarrow 0} \frac{1}{h} \int_{\Omega} \int_0^h \phi(\tilde{\mathbf{a}}, \nabla \tilde{\mathbf{a}}; \mathbf{c} + r\tilde{\mathbf{c}}) dr d\mathbf{x} \\
&= \int_{\Omega} \phi(\tilde{\mathbf{a}}, \nabla \tilde{\mathbf{a}}; \mathbf{c}) d\mathbf{x},
\end{aligned}$$

where the change of variable $r = hs$ has been used. Using this result in equation (17) leads to the first-order stability condition

$$\delta \mathcal{E}(\mathbf{q})(\tilde{\mathbf{q}}) + \mathcal{R}(\tilde{\mathbf{a}}; \mathbf{q}) - \int_{\Omega} \rho \mathbf{b} \cdot \tilde{\mathbf{u}} d\mathbf{x} - \int_{\Gamma_N} \bar{\mathbf{t}} \cdot \tilde{\mathbf{u}} dS \geq 0, \quad \forall \tilde{\mathbf{q}} \in \tilde{\mathcal{Q}}, \quad (19)$$

where $\delta \mathcal{E}(\mathbf{q})(\tilde{\mathbf{q}})$ is the Gâteaux derivative of \mathcal{E} in the direction $\tilde{\mathbf{q}}$. Equation (19) is a necessary condition for directional stability (15) that becomes sufficient if the inequality is strict. Otherwise, the study of higher-order conditions is required [23, 24, 78, 79], which is out of scope in the present study. Furthermore, if the energy quantities in the energy balance (14) are sufficiently regular in $[0, t]$, the time derivative of (14) yields the power balance equation

$$\frac{d}{dt} \mathcal{E}(\mathbf{q}) + \mathcal{R}(\dot{\mathbf{a}}; \mathbf{q}) - \int_{\Omega} \rho \mathbf{b} \cdot \dot{\mathbf{u}} d\mathbf{x} - \int_{\Gamma_N} \bar{\mathbf{t}} \cdot \dot{\mathbf{u}} dS - \int_{\Gamma_D} \mathbf{t}_r \cdot \dot{\mathbf{u}} dS = 0. \quad (20)$$

Dissipation inequality. To ensure physical soundness, a dissipation inequality is included in the formulation [73], ensuring the fulfilment of the second law of thermodynamics:

$$\phi(\dot{\mathbf{a}}, \nabla \dot{\mathbf{a}}; \mathbf{c}) \geq 0 \quad \text{in } \Omega \times \mathbb{T}. \quad (21)$$

Governing equations. Using equations (7)–(10), and in view of the stress-strain relation (3), the first-order stability condition (19) yields

$$\begin{aligned}
\int_{\Omega} \{ \delta_{\mathbf{a}} \psi(\boldsymbol{\varepsilon}, \mathbf{a}, \nabla \mathbf{a}) + \delta_{\tilde{\mathbf{a}}} \phi(\tilde{\mathbf{a}}, \nabla \tilde{\mathbf{a}}; \mathbf{c}) \} \cdot \tilde{\mathbf{a}} d\mathbf{x} + \int_{\Gamma} \{ \mathbf{n} \cdot (\partial_{\nabla \tilde{\mathbf{a}}} \phi(\tilde{\mathbf{a}}, \nabla \tilde{\mathbf{a}}; \mathbf{c}) + \partial_{\nabla \mathbf{a}} \psi(\boldsymbol{\varepsilon}, \mathbf{a}, \nabla \mathbf{a})) \} \cdot \tilde{\mathbf{a}} dS \\
- \int_{\Omega} (\operatorname{div} \boldsymbol{\sigma} + \rho \mathbf{b}) \cdot \tilde{\mathbf{u}} d\mathbf{x} + \int_{\Gamma_N} (\boldsymbol{\sigma} \cdot \mathbf{n} - \bar{\mathbf{t}}) \cdot \tilde{\mathbf{u}} dS \geq 0,
\end{aligned} \quad (22)$$

which holds for all $\tilde{\mathbf{q}} \in \tilde{\mathcal{Q}}$. Likewise, the power balance (20) gives

$$\begin{aligned}
\int_{\Omega} \{ \delta_{\mathbf{a}} \psi(\boldsymbol{\varepsilon}, \mathbf{a}, \nabla \mathbf{a}) + \delta_{\dot{\mathbf{a}}} \phi(\dot{\mathbf{a}}, \nabla \dot{\mathbf{a}}; \mathbf{c}) \} \cdot \dot{\mathbf{a}} d\mathbf{x} + \int_{\Gamma} \{ \mathbf{n} \cdot (\partial_{\nabla \dot{\mathbf{a}}} \phi(\dot{\mathbf{a}}, \nabla \dot{\mathbf{a}}; \mathbf{c}) + \partial_{\nabla \mathbf{a}} \psi(\boldsymbol{\varepsilon}, \mathbf{a}, \nabla \mathbf{a})) \} \cdot \dot{\mathbf{a}} dS \\
- \int_{\Omega} (\operatorname{div} \boldsymbol{\sigma} + \rho \mathbf{b}) \cdot \dot{\mathbf{u}} d\mathbf{x} + \int_{\Gamma_N} (\boldsymbol{\sigma} \cdot \mathbf{n} - \bar{\mathbf{t}}) \cdot \dot{\mathbf{u}} dS + \int_{\Gamma_D} (\boldsymbol{\sigma} \cdot \mathbf{n} - \mathbf{t}_r) \cdot \dot{\mathbf{u}} dS = 0.
\end{aligned} \quad (23)$$

Equations (22) and (23) yield:

$$\left\{ \begin{array}{l} \operatorname{div} \boldsymbol{\sigma} + \rho \mathbf{b} = \mathbf{0} \quad \text{in } \Omega, \\ \boldsymbol{\sigma} \cdot \mathbf{n} = \bar{\mathbf{t}} \quad \text{on } \Gamma_N, \\ \boldsymbol{\sigma} \cdot \mathbf{n} = \mathbf{t}_t \quad \text{on } \Gamma_D, \end{array} \right. \quad \text{and} \quad \left\{ \begin{array}{l} -\delta_{\mathbf{a}} \psi(\boldsymbol{\varepsilon}, \mathbf{a}, \nabla \mathbf{a}) - \delta_{\bar{\mathbf{a}}} \phi(\bar{\mathbf{a}}, \nabla \bar{\mathbf{a}}; \mathbf{c}) \leq \mathbf{0} \quad \text{in } \Omega, \\ \{ -\delta_{\dot{\mathbf{a}}} \psi(\boldsymbol{\varepsilon}, \mathbf{a}, \nabla \mathbf{a}) - \delta_{\dot{\mathbf{a}}} \phi(\dot{\mathbf{a}}, \nabla \dot{\mathbf{a}}; \mathbf{c}) \} \cdot \dot{\mathbf{a}} = 0 \quad \text{in } \Omega, \\ \nabla \mathbf{a} \cdot \mathbf{n} = \mathbf{0} \quad \text{on } \Gamma, \end{array} \right. \quad (24)$$

encompassing the equilibrium equations (1) and the evolution equations (5) for the internal variables. Note that boundary conditions for internal variables are also recovered.

2.4. Incremental minimization problem

An incremental minimization problem suitable for numerical implementation naturally follows from the global energetic formulation [72]. Consider $n_t + 1$ discrete time instants $0 = t_0 < \dots < t_n < t_{n+1} < \dots < t_{n_t} = t_{\max}$. Using equation (16), the incremental dissipated energy up to t_{n+1} reads

$$\mathcal{D}(\mathbf{q}_0, \mathbf{q}_{n+1}) = \mathcal{D}(\mathbf{q}_0, \mathbf{q}_n) + \mathcal{D}(\mathbf{q}_n, \mathbf{q}_{n+1}). \quad (25)$$

The goal is to evaluate the dissipated energy increment from t_n to t_{n+1} , which follows from (12) as

$$\mathcal{D}(\mathbf{q}_n, \mathbf{q}_{n+1}) = \int_{\Omega} \int_{t_n}^{t_{n+1}} \phi \left(\frac{\mathbf{a}_{n+1} - \mathbf{a}_n}{t_{n+1} - t_n}, \frac{\nabla \mathbf{a}_{n+1} - \nabla \mathbf{a}_n}{t_{n+1} - t_n}; \mathbf{c}_n + \frac{t - t_n}{t_{n+1} - t_n} (\mathbf{c}_{n+1} - \mathbf{c}_n) \right) dt d\mathbf{x}. \quad (26)$$

In some cases, the dissipation potential is such that the dissipated energy is a state function. For this to occur, it is necessary (but not sufficient) that $\mathcal{D}(\mathbf{q}_n, \mathbf{q}_{n+1}) \equiv \mathcal{D}(\mathbf{a}_n, \mathbf{a}_{n+1})$. In other words, the dissipation potential must not depend on the non-dissipative state variables. Then, the evaluation of (26) is straightforward and equivalent to the direct computation of the dissipated energy $\int_{t_n}^{t_{n+1}} \mathcal{R}(\dot{\mathbf{a}}(\tau); \mathbf{a}(\tau)) d\tau$. In the model presented in section 3, we shall see that only part of the dissipated energy is a state function.

In the more general case where the dissipated energy is not a state function, as is often the case for state-dependent dissipation potentials (e.g., in non-associative plasticity), an incremental approximation is required to evaluate the time integral in (26). Taking the zeroth-order term of a Taylor expansion of the integral kernel (noting that all other terms imply rate-dependence), equation (26) is approximated as

$$\mathcal{D}(\mathbf{q}_n, \mathbf{q}_{n+1}) \approx \mathcal{R}(\mathbf{a}_{n+1} - \mathbf{a}_n; \mathbf{q}_n) =: \mathcal{D}(\mathbf{a}_n, \mathbf{a}_{n+1}; \mathbf{q}_n). \quad (27)$$

This expression represents an explicit approximation of the state-dependent dissipated energy, in agreement with the incremental framework of Miehe [15] (see also Mielke and Rossi [87] and Luege et al. [76]).¹

Given all states up to t_n , the unknown state \mathbf{q}_{n+1} is found from the variational principle

$$\inf_{\mathbf{q}_{n+1} \in \mathcal{Q}} \{ \mathcal{E}(\mathbf{q}_{n+1}) - \mathcal{T}(\mathbf{u}_n, \mathbf{u}_{n+1}) + \mathcal{D}(\mathbf{a}_n, \mathbf{a}_{n+1}; \mathbf{q}_n) \}, \quad (28)$$

where the dissipation inequality (21) must be enforced in incremental form.

¹Other approximations involving implicit schemes are also possible; see Stainier [88] and Brassart et al. [89].

The incremental minimization problem (28) directly recovers the continuous evolution problem (24) when the dissipated energy is a state function [90, 91]. In particular, stationarity of the total energy at t_{n+1} implies the first-order stability condition (19), while taking the limit as $t_{n+1} - t_n \rightarrow 0$ allows to recover the energy balance (20). Similarly, one can show the link between the continuous and incremental problems for the general case in which the dissipated energy is not a state function [76]. As will become clear in section 3, this link is not as straightforward as for the path-independent counterpart; nevertheless, it suffices to ensure that the incremental dissipation (27) is such that the Euler-Lagrange equations of (28) recover the continuous evolution problem (24) as $t_{n+1} - t_n \rightarrow 0$ (see Stainier [88] for a deeper discussion on this topic).

2.5. Overview

Table 1 presents an overview of the present variational formulation. In the following section, the abstract setting presented so far will take specific form after defining the state variables, the free energy density and the dissipation potential.

Table 1. Constitutive energy functionals, energetic formulation and incremental energy minimization.

Constitutive energy functionals	
Stored energy	$\mathcal{E}(\mathbf{q}) = \int_{\Omega} \psi(\boldsymbol{\varepsilon}, \mathbf{a}, \nabla \mathbf{a}) \, d\mathbf{x}$
Dissipative power	$\mathcal{R}(\dot{\mathbf{a}}; \mathbf{q}) = \int_{\Omega} \phi(\dot{\mathbf{a}}, \nabla \dot{\mathbf{a}}; \mathbf{c}) \, d\mathbf{x}$, with $\phi(\dot{\mathbf{a}}, \nabla \dot{\mathbf{a}}; \mathbf{c}) \geq 0$
Incremental dissipated energy	$\mathcal{D}(\mathbf{a}_{n+1}, \mathbf{a}_n; \mathbf{q}_n)$, from (26) or (27)
Continuous evolution problem	
Energy balance (20)	$\frac{d}{dt} \mathcal{E}(\mathbf{q}) + \mathcal{R}(\dot{\mathbf{a}}; \mathbf{q}) - \int_{\Omega} \rho \mathbf{b} \cdot \dot{\mathbf{u}} \, d\mathbf{x} - \int_{\Gamma_N} \bar{\mathbf{t}} \cdot \dot{\mathbf{u}} \, dS - \int_{\Gamma_D} \mathbf{t}_r \cdot \dot{\mathbf{u}} \, dS = 0$
Stability (19)	$\delta \mathcal{E}(\mathbf{q})(\bar{\mathbf{q}}) + \mathcal{R}(\bar{\mathbf{a}}; \mathbf{q}) - \int_{\Omega} \rho \mathbf{b} \cdot \bar{\mathbf{u}} \, d\mathbf{x} - \int_{\Gamma_N} \bar{\mathbf{t}} \cdot \bar{\mathbf{u}} \, dS \geq 0$
Incremental evolution problem	
Incremental minimization (28)	$\inf_{\mathbf{q}_{n+1} \in \mathcal{Q}} \{ \mathcal{E}(\mathbf{q}_{n+1}) - \mathcal{T}(\mathbf{u}_n, \mathbf{u}_{n+1}) + \mathcal{D}(\mathbf{a}_n, \mathbf{a}_{n+1}; \mathbf{q}_n) \}$

3. A phase-field model with fatigue effects coupled to cyclic plasticity

This section presents the proposed model that couples a phase-field approach to fatigue with cyclic plasticity, derived using the concepts presented in section 2. First, the modeling of cyclic plasticity is addressed, where a non-associative ratcheting variable is introduced in the variational framework. Then, the full model is elaborated by introducing the phase-field description of fatigue-induced fracture.

3.1. Modeling cyclic plasticity with ratcheting

To account for cyclic plasticity with ratcheting effects, we take the model of Houlsby et al. [52] as a point of departure, which was proposed to describe the behavior of cyclically loaded pile foundations [92].

The original model is tightly linked to Armstrong and Frederick [53], but allows for multi-surface kinematic hardening with a single ratcheting variable. Herein, we also consider isotropic hardening/softening and gradient-extended plasticity [67, 68, 93–95], accounting for a general class of elastoplastic materials.

To present the model, we adopt the conventional setting of plasticity, where auxiliary internal variables are introduced to account for hardening effects [96, 97] and, in this case, ratcheting. As in classical elastoplasticity, the evolution of the internal variables is first presented in dual form, that is, in terms of yield functions in generalized-stress space, where the issue of associativity is addressed. Then, a state-dependent primal dissipation potential is obtained, which is used to construct the coupled fatigue model in section 3.2.

3.1.1. Constitutive model

We focus on a multi-surface representation of the plastic deformation process, with $n_y \geq 1$ yield surfaces of increasing yield strength. To this end, we introduce the internal variables

$$\{\boldsymbol{\varepsilon}^P, \boldsymbol{\kappa}, \boldsymbol{\varepsilon}^r\}, \quad \text{with} \quad \boldsymbol{\varepsilon}^P := \{\boldsymbol{\varepsilon}_1^P, \dots, \boldsymbol{\varepsilon}_s^P, \dots, \boldsymbol{\varepsilon}_{n_y}^P\} \quad \text{and} \quad \boldsymbol{\kappa} := \{\kappa_1, \dots, \kappa_s, \dots, \kappa_{n_y}\}. \quad (29)$$

The subscript s denotes the s^{th} yield surface with a corresponding plastic strain tensor $\boldsymbol{\varepsilon}_s^P: \Omega \times \mathbb{T} \rightarrow \mathbb{R}_{\text{dev}}^{d \times d} := \{\boldsymbol{e} \in \mathbb{R}_{\text{sym}}^{d \times d} \mid \text{tr}(\boldsymbol{e}) = 0\}$ and an isotropic hardening/softening variable $\kappa_s: \Omega \times \mathbb{T} \rightarrow \mathbb{R}_+$, and $\boldsymbol{\varepsilon}^r: \Omega \times \mathbb{T} \rightarrow \mathbb{R}_{\text{dev}}^{d \times d}$ is a ratcheting strain tensor. As a modeling assumption, κ_s evolves according to the hardening law

$$\dot{\kappa}_s := \sqrt{\frac{2}{3}} \|\dot{\boldsymbol{\varepsilon}}_s^P\|. \quad (30)$$

The ratcheting strain tensor $\boldsymbol{\varepsilon}^r$ evolves according to the ratcheting law

$$\dot{\boldsymbol{\varepsilon}}^r := \beta \hat{\boldsymbol{r}} \sum_{s=1}^{n_y} \|\dot{\boldsymbol{\varepsilon}}_s^P\|, \quad (31)$$

where $\hat{\boldsymbol{r}} := \partial \|\boldsymbol{\sigma}_{\text{dev}}\|$ is the direction of the deviatoric stress [52]. The parameter $\beta \in [0, 1]$ defines the fraction of plastic strains that contributes to ratcheting, assumed, for simplicity, to be equal for all yield surfaces.

In light of the internal variables defined above, we shall present the plasticity model in the multi-surface setting, in agreement with the ratcheting model of Houlsby et al. [52]. This choice has been made to favor generality and to endow the model with great flexibility to accommodate different material responses. Note that throughout the sequel, the single-surface case can always be recovered, where $n_y = 1$.

The free energy density is defined as

$$\psi(\boldsymbol{\varepsilon}, \boldsymbol{\varepsilon}^P, \boldsymbol{\kappa}, \boldsymbol{\varepsilon}^r, \nabla \boldsymbol{\kappa}) := \underbrace{\frac{1}{2} \|\boldsymbol{\varepsilon} - \sum_{s=1}^{n_y} \boldsymbol{\varepsilon}_s^P - \boldsymbol{\varepsilon}^r\|_{\mathbf{C}}^2}_{\psi^e(\boldsymbol{\varepsilon}, \boldsymbol{\varepsilon}^P, \boldsymbol{\varepsilon}^r)} + \underbrace{\frac{1}{2} \sum_{s=1}^{n_y} (H_s^{\text{kin}} \boldsymbol{\varepsilon}_s^P : \boldsymbol{\varepsilon}_s^P + H_s^{\text{iso}} \kappa_s^2)}_{\psi^P(\boldsymbol{\varepsilon}^P, \boldsymbol{\kappa}, \nabla \boldsymbol{\kappa})} + \frac{1}{2} \sum_{s=1}^{n_y} \eta_{ps}^2 \|\nabla \kappa_s\|^2, \quad (32)$$

where \mathbf{C} is the fourth-order elastic tensor. H_s^{kin} and H_s^{iso} denote the kinematic and isotropic hardening moduli, respectively, for the s^{th} yield surface. The last term in equation (32) introduces non-local effects governed by the plastic internal length scale η_{ps} , which is related to the plastic characteristic length ℓ_{ps} by

$$\eta_{ps} = \ell_{ps} \sqrt{\sigma_s^P}, \quad (33)$$

where σ_s^p is the s^{th} plastic yield strength (cf. [98] for the single-surface case). Note that in contrast with η_{ps} , ℓ_{ps} has the units of length.

In view of equation (32), the stress tensor is obtained from equation (3) as

$$\boldsymbol{\sigma}(\boldsymbol{\varepsilon}, \boldsymbol{\varepsilon}^p, \boldsymbol{\varepsilon}^r) = \frac{\partial \psi}{\partial \boldsymbol{\varepsilon}} = \mathbf{C} : \left(\boldsymbol{\varepsilon} - \sum_{s=1}^{n_y} \boldsymbol{\varepsilon}_s^p - \boldsymbol{\varepsilon}^r \right). \quad (34)$$

The generalized stresses conjugate to (29) read

$$\{\mathbf{s}^p, \mathbf{h}, \mathbf{s}^r\}, \quad \text{with} \quad \mathbf{s}^p := \{\mathbf{s}_1^p, \dots, \mathbf{s}_s^p, \dots, \mathbf{s}_{n_y}^p\} \quad \text{and} \quad \mathbf{h} := \{h_1, \dots, h_s, \dots, h_{n_y}\}. \quad (35)$$

These dual variables follow from equation (4) as

$$\mathbf{s}_s^p = -\delta_{\boldsymbol{\varepsilon}_s^p} \psi \equiv \boldsymbol{\sigma} - H_s^{\text{kin}} \boldsymbol{\varepsilon}_s^p, \quad h_s = -\delta_{\kappa_s} \psi \equiv -H_s^{\text{iso}} \kappa_s + \eta_{ps}^2 \text{div}[\nabla \kappa_s], \quad \mathbf{s}^r = -\delta_{\boldsymbol{\varepsilon}^r} \psi \equiv \boldsymbol{\sigma}. \quad (36)$$

3.1.2. Dissipation

Focusing on J_2 plasticity, the yield functions are defined in generalized-stress space as

$$f_s^p(\mathbf{s}_s^p, h_s) := \|\mathbf{s}_{s \text{ dev}}^p\| - \sqrt{\frac{2}{3}}(\sigma_s^p - h_s) \leq 0. \quad (37)$$

The set of admissible generalized stresses for each yield surface is the convex set

$$\mathbb{K}_s := \{\mathbf{s}_s^p, h_s, \mathbf{s}^r \mid f_s^p(\mathbf{s}_s^p, h_s) \leq 0\},$$

such that the elastic domain is the intersection of all \mathbb{K}_s , and thus still a convex set:

$$\mathbb{K} := \bigcap_{s=1}^{n_y} \mathbb{K}_s = \{\mathbf{s}^p, \mathbf{h}, \mathbf{s}^r \mid f_s^p(\mathbf{s}_s^p, h_s) \leq 0 \forall s \in \mathbf{Y}\}, \quad (38)$$

where $\mathbf{Y} := \mathbb{Z} \cap [1, n_y]$. To obtain the primal representation of the dissipation power in the case of associative models, the dissipation potential is obtained as the support function of \mathbb{K} for given rates $\{\dot{\boldsymbol{\varepsilon}}^p, \dot{\boldsymbol{\kappa}}, \dot{\boldsymbol{\varepsilon}}^r\}$:

$$\phi = \sup\{\tilde{\mathbf{s}}^p : \dot{\boldsymbol{\varepsilon}}^p + \tilde{\mathbf{h}} \cdot \dot{\boldsymbol{\kappa}} + \tilde{\mathbf{s}}^r : \dot{\boldsymbol{\varepsilon}}^r \mid \{\tilde{\mathbf{s}}^p, \tilde{\mathbf{h}}, \tilde{\mathbf{s}}^r\} \in \mathbb{K}\}. \quad (39)$$

This optimization problem can be viewed as a particular statement of the principle of maximum dissipation. Equation (39) yields as necessary conditions the associative flow rule for the plastic strains, as well as the associative hardening law, consistent with equation (30) and the normality law [55, 61]:

$$\dot{\boldsymbol{\varepsilon}}_s^p = \sum_{k=1}^{n_y} \lambda_k \frac{\partial f_k^p}{\partial \mathbf{s}_s^p} \equiv \lambda_s \hat{\mathbf{n}}_s, \quad \dot{\kappa}_s = \sum_{k=1}^{n_y} \lambda_k \frac{\partial f_k^p}{\partial h_s} \equiv \sqrt{\frac{2}{3}} \lambda_s, \quad (40)$$

where $\lambda_s \geq 0$, and $\hat{\mathbf{n}}_s := \mathbf{s}_{s \text{ dev}}^p / \|\mathbf{s}_{s \text{ dev}}^p\|$ is the direction of the plastic flow. However, the fact that $\partial_{\mathbf{s}^r} f_s^p = \mathbf{0}$ implies that $\dot{\boldsymbol{\varepsilon}}^r \equiv \mathbf{0}$. Therefore, the ratcheting law (31) is not obtained from (39) and is thus considered non-associative. Equation (39) then leads to a dissipation potential that is independent of the ratcheting strain rate and is thus inconsistent with the ratcheting model.

An approach to circumvent this issue and recover a variational structure in models with non-associative components is to let the set of admissible generalized stresses depend on the current state [83]. To this end, we define the set

$$\mathbb{L}(\mathbf{s}^r) := \{ \tilde{\mathbf{s}}^p, \tilde{\mathbf{h}}, \tilde{\mathbf{s}}^r \mid g_s^p(\tilde{\mathbf{s}}_s^p, \tilde{h}_s, \tilde{\mathbf{s}}^r) \leq \beta \|\mathbf{s}_{\text{dev}}^r\| \ \forall s \in Y \}, \quad (41)$$

where $g_s^p(\mathbf{s}_s^p, h_s, \mathbf{s}^r) := f_s^p(\mathbf{s}_s^p, h_s) + \beta \|\mathbf{s}_{\text{dev}}^r\|$. The dissipation potential then follows as the stress-dependent support function of $\mathbb{L}(\mathbf{s}^r)$:

$$\phi = \sup \{ \tilde{\mathbf{s}}^p : \dot{\boldsymbol{\epsilon}}^p + \tilde{\mathbf{h}} \cdot \dot{\boldsymbol{\kappa}} + \tilde{\mathbf{s}}^r : \dot{\boldsymbol{\epsilon}}^r \mid \{ \tilde{\mathbf{s}}^p, \tilde{\mathbf{h}}, \tilde{\mathbf{s}}^r \} \in \mathbb{L}(\mathbf{s}^r) \}. \quad (42)$$

Equation (42) yields as necessary conditions the evolution equations (40) as well as the ratcheting law

$$\dot{\boldsymbol{\epsilon}}^r = \sum_{s=1}^{n_y} \lambda_s \frac{\partial g_s}{\partial \mathbf{s}^r} \equiv \beta \hat{\mathbf{r}} \sum_{s=1}^{n_y} \lambda_s. \quad (43)$$

In equations (40) and (43), we note that the direction of the plastic flow for each yield surface coincides with the direction of the relative deviatoric stress $\mathbf{s}_{s \text{ dev}}^p$, while the direction of the ratcheting strain rate coincides with the direction of the deviatoric stress $\boldsymbol{\sigma}_{\text{dev}}$. In view of equations (30) and (31), equation (42) is evaluated for all $\{ \dot{\boldsymbol{\epsilon}}^p, \dot{\boldsymbol{\kappa}}, \dot{\boldsymbol{\epsilon}}^r \} \in \mathbb{R}_{\text{dev}}^{d \times d} \times \mathbb{R}_+ \times \mathbb{R}_{\text{dev}}^{d \times d}$ as

$$\begin{aligned} \phi(\dot{\boldsymbol{\epsilon}}^p, \dot{\boldsymbol{\kappa}}, \dot{\boldsymbol{\epsilon}}^r; \mathbf{s}^r) &= \sup \left\{ \tilde{\mathbf{s}}^p : \dot{\boldsymbol{\epsilon}}^p + \tilde{\mathbf{h}} \cdot \dot{\boldsymbol{\kappa}} + \tilde{\mathbf{s}}^r : \dot{\boldsymbol{\epsilon}}^r \mid g_s(\tilde{\mathbf{s}}_s^p, \tilde{h}_s, \tilde{\mathbf{s}}^r) \leq \beta \|\mathbf{s}_{\text{dev}}^r\| \ \forall s \in Y \right\} \\ &= \sup \left\{ \sum_{s=1}^{n_y} \left(\|\tilde{\mathbf{s}}_{s \text{ dev}}^p\| \|\dot{\boldsymbol{\epsilon}}_s^p\| + \tilde{h}_s \dot{\kappa}_s \right) + \|\tilde{\mathbf{s}}_{\text{dev}}^r\| \|\dot{\boldsymbol{\epsilon}}^r\| \mid \|\tilde{\mathbf{s}}_{s \text{ dev}}^p\| \leq \beta \|\mathbf{s}_{\text{dev}}^r\| - \sqrt{\frac{2}{3}}(\tilde{h}_s - \sigma_s^p) - \beta \|\tilde{\mathbf{s}}_{\text{dev}}^r\| \ \forall s \in Y \right\} \\ &= \sup \left\{ \sum_{s=1}^{n_y} \left[\left(\beta \|\mathbf{s}_{\text{dev}}^r\| - \sqrt{\frac{2}{3}}(\tilde{h}_s - \sigma_s^p) - \beta \|\tilde{\mathbf{s}}_{\text{dev}}^r\| \right) \|\dot{\boldsymbol{\epsilon}}_s^p\| + \tilde{h}_s \dot{\kappa}_s \right] + \|\tilde{\mathbf{s}}_{\text{dev}}^r\| \|\dot{\boldsymbol{\epsilon}}^r\| \right\} \\ &= \sup \left\{ \sum_{s=1}^{n_y} \left[\left(\sqrt{\frac{2}{3}} \sigma_s^p + \beta \|\mathbf{s}_{\text{dev}}^r\| \right) \|\dot{\boldsymbol{\epsilon}}_s^p\| + \tilde{h}_s \left(\dot{\kappa}_s - \sqrt{\frac{2}{3}} \|\dot{\boldsymbol{\epsilon}}_s^p\| \right) \right] + \|\tilde{\mathbf{s}}_{\text{dev}}^r\| \left(\|\dot{\boldsymbol{\epsilon}}^r\| - \beta \sum_{s=1}^{n_y} \|\dot{\boldsymbol{\epsilon}}_s^p\| \right) \right\}. \end{aligned}$$

The expression inside the supremum becomes unbounded if the term multiplying $\|\tilde{\mathbf{s}}_{\text{dev}}^r\|$ is positive. Moreover, for isotropic hardening plasticity, $\tilde{h}_s \leq 0$, such that the expression inside the supremum becomes unbounded if the term multiplying \tilde{h}_s is negative. The dissipation potential then takes the closed form

$$\phi(\dot{\boldsymbol{\epsilon}}^p, \dot{\boldsymbol{\kappa}}, \dot{\boldsymbol{\epsilon}}^r; \mathbf{s}^r) = \begin{cases} \sum_{s=1}^{n_y} \left(\sqrt{\frac{2}{3}} \sigma_s^p + \beta \|\mathbf{s}_{\text{dev}}^r\| \right) \|\dot{\boldsymbol{\epsilon}}_s^p\| & \text{if } \dot{\kappa}_s \geq \sqrt{\frac{2}{3}} \|\dot{\boldsymbol{\epsilon}}_s^p\| \text{ and } \|\dot{\boldsymbol{\epsilon}}^r\| \leq \beta \sum_{s=1}^{n_y} \|\dot{\boldsymbol{\epsilon}}_s^p\|, \\ +\infty & \text{otherwise.} \end{cases} \quad (44)$$

A similar result follows in case of isotropic softening. Expression (44) is consistent with the dissipation potential proposed by Houlsby et al. [52] (without isotropic hardening) in the context of hyperplasticity, a topic strongly linked to generalized standard materials [85].

3.2. Coupling cyclic plasticity to a phase-field approach to fatigue

3.2.1. Constitutive model

The formulation is now extended, coupling the cyclic plasticity model to a phase-field description of fatigue fracture. For this purpose, the usual phase-field/damage variable is defined as $\alpha: \Omega \times \mathbb{T} \rightarrow [0, 1]$,

with $\alpha = 0$ and $\alpha = 1$ corresponding to an undamaged and a fully degraded material state, respectively. Regularization is attained by the gradient of the phase field $\nabla\alpha: \Omega \times \mathbb{T} \rightarrow \mathbb{R}^d$. Then, along with the plastic variables introduced in the previous section, the constitutive state reads

$$\mathbf{c} := \{\boldsymbol{\varepsilon}, \boldsymbol{\varepsilon}^p, \boldsymbol{\kappa}, \boldsymbol{\varepsilon}^r, \alpha, \nabla\boldsymbol{\kappa}, \nabla\alpha\},$$

with primary fields

$$\mathbf{q} := \{\mathbf{u}, \boldsymbol{\varepsilon}^p, \boldsymbol{\kappa}, \boldsymbol{\varepsilon}^r, \alpha\}.$$

The damage variable is considered irreversible, thus excluding healing:

$$\dot{\alpha} \geq 0 \quad \text{in} \quad \Omega \times \mathbb{T}. \quad (45)$$

Note that from the hardening law (30), it follows that $\kappa_s \in \boldsymbol{\kappa}$ is also irreversible by definition.

Material degradation is achieved by letting the free energy density decrease as a function of α :

$$\psi(\boldsymbol{\varepsilon}, \boldsymbol{\varepsilon}^p, \boldsymbol{\kappa}, \boldsymbol{\varepsilon}^r, \alpha, \nabla\boldsymbol{\kappa}) := g(\alpha)(\psi^{e+}(\boldsymbol{\varepsilon}, \boldsymbol{\varepsilon}^p, \boldsymbol{\varepsilon}^r) + \psi^p(\boldsymbol{\varepsilon}^p, \boldsymbol{\kappa}, \nabla\boldsymbol{\kappa})) + \psi^{e-}(\boldsymbol{\varepsilon}, \boldsymbol{\varepsilon}^p, \boldsymbol{\varepsilon}^r), \quad (46)$$

where $g(\alpha)$ is a damage degradation function endowed with the following properties:

$$g(0) = 1, \quad g(1) = 0, \quad g'(\alpha) \leq 0 \quad \forall \alpha \in [0, 1]. \quad (47)$$

In this work, the widely used quadratic function is adopted:

$$g(\alpha) := (1 - \alpha)^2. \quad (48)$$

In equation (46), ψ^p is the plastic free energy density given in equation (32). On the other hand, the elastic free energy is split into damageable and undamageable parts, denoted as ψ^{e+} and ψ^{e-} , respectively. This decomposition is introduced to consider asymmetric behavior in tension and compression, and can be performed in different ways. Herein, we consider the volumetric-deviatoric split [99]:

$$\begin{cases} \psi^{e+}(\boldsymbol{\varepsilon}, \boldsymbol{\varepsilon}^p, \boldsymbol{\varepsilon}^r) := \frac{1}{2}K \langle \text{tr}(\boldsymbol{\varepsilon}^e) \rangle_+^2 + \mu(\boldsymbol{\varepsilon}_{\text{dev}}^e : \boldsymbol{\varepsilon}_{\text{dev}}^e), \\ \psi^{e-}(\boldsymbol{\varepsilon}, \boldsymbol{\varepsilon}^p, \boldsymbol{\varepsilon}^r) := \frac{1}{2}K \langle \text{tr}(\boldsymbol{\varepsilon}^e) \rangle_-^2, \end{cases} \quad (49)$$

where K is the bulk modulus, μ is the shear modulus, and

$$\boldsymbol{\varepsilon}^e := \boldsymbol{\varepsilon} - \sum_{s=1}^{n_y} \boldsymbol{\varepsilon}_s^p - \boldsymbol{\varepsilon}^r \quad (50)$$

is the elastic strain tensor. From the decomposed energy density (46), the stress-strain relation (3) reads

$$\boldsymbol{\sigma}(\boldsymbol{\varepsilon}, \boldsymbol{\varepsilon}^p, \boldsymbol{\varepsilon}^r, \alpha) = \frac{\partial\psi}{\partial\boldsymbol{\varepsilon}} = g(\alpha) \frac{\partial\psi^{e+}}{\partial\boldsymbol{\varepsilon}} + \frac{\partial\psi^{e-}}{\partial\boldsymbol{\varepsilon}}. \quad (51)$$

3.2.2. Dissipation

The definition of the dissipation potential should entail coupling of the plastic strains to damage evolution, for which we follow the approaches in references [30, 37, 38, 77, 84], and extend the formulation to multiple yield surfaces, kinematic hardening and ratcheting. Moreover, following Alessi et al. [12] and Carrara et al. [13], fatigue effects are considered by means of a local fatigue variable, defined here as $\gamma: \Omega \times \mathbb{T} \rightarrow \mathbb{R}_+$, and a fatigue degradation function $\gamma \mapsto d(\gamma) \in [0, 1]$. This function has the following properties:

$$d(\gamma \leq \gamma_0) = 1, \quad d(\gamma > \gamma_0) \in [0, 1], \quad d'(\gamma) \leq 0, \quad (52)$$

where γ_0 is a material threshold parameter.

The different dissipative ingredients are introduced in the following dissipation potential:

$$\phi(\dot{\boldsymbol{\varepsilon}}^p, \dot{\boldsymbol{\kappa}}, \dot{\boldsymbol{\varepsilon}}^r, \dot{\alpha}, \nabla \dot{\alpha}; \boldsymbol{\kappa}, \alpha, \boldsymbol{\sigma}, \gamma) := \underbrace{\phi^p(\dot{\boldsymbol{\varepsilon}}^p, \dot{\boldsymbol{\kappa}}, \dot{\boldsymbol{\varepsilon}}^r; \alpha, \nabla \alpha, \boldsymbol{\sigma})}_{\text{plastic dissipation}} + \sum_{s=1}^{n_y} \underbrace{g'(\alpha) \sigma_s^p \kappa_s \dot{\alpha}}_{\text{coupling}} + \underbrace{\phi^d(\dot{\alpha}, \nabla \dot{\alpha}; \alpha, \nabla \alpha, \gamma)}_{\text{damage dissipation}}. \quad (53)$$

The coupling term $g'(\alpha) \kappa_s \dot{\alpha}$ was introduced by Alessi et al. [31] for perfect plasticity to render the dissipated energy a state function. This idea is also applied here and generalized to the multi-surface hardening case. However, due to the dependence on $\boldsymbol{\sigma}$ and γ , only part of the dissipated energy becomes a state function. The plastic dissipation corresponds to the damaged version of equation (44):

$$\phi^p(\dot{\boldsymbol{\varepsilon}}^p, \dot{\boldsymbol{\kappa}}, \dot{\boldsymbol{\varepsilon}}^r; \alpha, \boldsymbol{\sigma}) = \sum_{s=1}^{n_y} \left(\sqrt{\frac{2}{3}} g(\alpha) \sigma_s^p + \beta \|\boldsymbol{\sigma}_{\text{dev}}(\boldsymbol{\varepsilon}, \boldsymbol{\varepsilon}^p, \boldsymbol{\varepsilon}^r, \alpha)\| \right) \|\dot{\boldsymbol{\varepsilon}}_s^p\|. \quad (54)$$

In this expression, we have enforced the constraints that are present in (44) by assuming the hardening and ratcheting laws (30) and (31), as will be done hereinafter to simplify the presentation. The degradation function $g(\alpha)$ is used to let the plastic yield strength decrease as a function of damage. More general choices of functions that comply with (47) are possible. Herein, we only consider the quadratic function (48). The phase-field fracture dissipation potential with fatigue effects reads

$$\phi^d(\dot{\alpha}, \nabla \dot{\alpha}; \alpha, \nabla \alpha, \gamma) := d(\gamma) (w'(\alpha) \dot{\alpha} + \eta_d^2 \nabla \alpha \cdot \nabla \dot{\alpha}), \quad (55)$$

where η_d is the damage internal length scale. The terms $w'(\alpha) \dot{\alpha} + \eta_d^2 \nabla \alpha \cdot \nabla \dot{\alpha}$ constitute the standard phase-field dissipation power, whose time integral yields the regularized fracture energy density. This quantity is subject to degradation through $d(\gamma)$, which introduces a path-dependent fatigue effect. The function $w(\alpha)$ represents the local dissipated energy due to damage, for which two models (labeled AT-1 and AT-2 after Ambrosio and Tortorelli [100]) are generally adopted [24]:

$$w(\alpha) := \begin{cases} w_0 \alpha & \text{AT-1,} \\ w_0 \alpha^2 & \text{AT-2.} \end{cases} \quad (56)$$

With these definitions, the damage characteristic length ℓ_d can be recovered from the relation

$$\eta_d = \ell_d \sqrt{2w_0}. \quad (57)$$

While the AT-2 model is used in most studies, the AT-1 model has the advantage of including an initial elastic stage before damage is triggered, where w_0 is a threshold parameter [24, 37]. Regarding the fatigue degradation function, different options have been proposed [12, 13], from which we adopt the following:

$$d(\gamma) := \begin{cases} 1 & \text{if } \gamma(\mathbf{x}, t) \leq \gamma_0, \\ \left[1 - k \log\left(\frac{\gamma(\mathbf{x}, t)}{\gamma_0}\right)\right]^2 & \text{if } \gamma_0 \leq \gamma(\mathbf{x}, t) \leq \gamma_0 10^{1/k}, \\ 0 & \text{otherwise,} \end{cases} \quad (58)$$

where k is a material parameter that controls the rate of (logarithmic) decay of the fatigue degradation function. The fatigue variable γ is defined as

$$\gamma(\mathbf{x}, t) := \int_0^t \dot{\vartheta}(\mathbf{x}, s) H(\dot{\vartheta}(\mathbf{x}, s)) ds, \quad \text{with } \vartheta(\mathbf{x}, t) := g(\alpha) (\psi^{e+}(\boldsymbol{\varepsilon}, \boldsymbol{\varepsilon}^p, \boldsymbol{\varepsilon}^r) + \psi^p(\boldsymbol{\varepsilon}^p, \boldsymbol{\kappa}, \nabla \boldsymbol{\kappa})). \quad (59)$$

While other definitions are possible for ϑ , e.g., an accumulated strain measure, using the strain energy density ensures mesh-objectivity [13]. Moreover, the Heaviside function H precludes fatigue degradation in unloading stages. Note that in the present model, the plastic free energy also contributes to the evolution of γ .

Table 2 presents a summary of the different mechanisms included in the present model. In the following subsections, these definitions will be used to derive the evolution problem according to the formulation elaborated in section 2 (see table 1).

Table 2. State variables and parameters included in the multifield phase-field-based fatigue model with cyclic plasticity. These variables enter the free energy density (46) and the dissipation potential (53), which in turn constitute the basic ingredients of the energetic formulation summarized in table 1.

	Variable	Type	
ELASTICITY	Displacements	\mathbf{u}	Independent
	Strains	$\boldsymbol{\varepsilon}$	Dependent
PLASTICITY	Plastic strains	$\boldsymbol{\varepsilon}^p = \{\boldsymbol{\varepsilon}_1^p, \dots, \boldsymbol{\varepsilon}_s^p, \dots, \boldsymbol{\varepsilon}_{n_y}^p\}$	Independent
	Hardening/softening variables	$\boldsymbol{\kappa} = \{\kappa_1, \dots, \kappa_s, \dots, \kappa_{n_y}\}$	Dependent, irreversible
	Ratcheting strains	$\boldsymbol{\varepsilon}^r$	Dependent
	Plastic gradients	$\nabla \boldsymbol{\kappa} = \{\nabla \kappa_1, \dots, \nabla \kappa_s, \dots, \nabla \kappa_{n_y}\}$	Dependent
DAMAGE	Phase-field/damage variable	α	Independent, irreversible
	Damage gradient	$\nabla \alpha$	Dependent
FATIGUE	Fatigue parameter	γ	History-dependent, irreversible

3.3. Energetic formulation

With the previous definitions, the governing equations of the proposed model can be derived from the principles of the energetic formulation. For this purpose, we define the space of displacement fields in

equation (6) by $\mathcal{F} := \mathbf{H}^1(\Omega; \mathbb{R}^d)$, and the following function spaces for the internal variables:

$$\mathcal{B} := \mathbf{L}^2(\Omega; \mathbb{R}_{\text{dev}}^{d \times d}), \quad \tilde{\mathcal{B}} \equiv \mathcal{B}, \quad (60)$$

$$\mathcal{K} := \mathbf{H}^1(\Omega; \mathbb{R}_+), \quad \tilde{\mathcal{K}}(\mathbf{b}) := \{z \in \mathcal{K} \mid z = \sqrt{2/3} \|\mathbf{b}\|, \mathbf{b} \in \tilde{\mathcal{B}}\}, \quad (61)$$

$$\mathcal{R} := \mathbf{L}^2(\Omega; \mathbb{R}_{\text{dev}}^{d \times d}), \quad \tilde{\mathcal{R}}(\mathbf{b}) := \{z \in \mathcal{R} \mid \|z\| = \beta \sum_{s=1}^{n_y} \|\mathbf{b}_s\|, \mathbf{b}_s \in \tilde{\mathcal{B}}, \mathbf{b}_s \in \mathbf{b}\}, \quad (62)$$

$$\mathcal{D} := \mathbf{H}^1(\Omega; [0, 1]), \quad \tilde{\mathcal{D}} := \mathbf{H}^1(\Omega; \mathbb{R}_+). \quad (63)$$

The admissible primary fields are then given by

$$\mathbf{q} = \{\mathbf{u}, \boldsymbol{\varepsilon}^p, \boldsymbol{\kappa}, \boldsymbol{\varepsilon}^r, \alpha\} \in \mathcal{Q} := \mathcal{U} \times \mathcal{P} \times \mathcal{D}, \quad \text{with} \quad \mathcal{P} := \mathcal{B} \times \cdots \times \mathcal{B} \times \mathcal{K} \times \cdots \times \mathcal{K} \times \mathcal{R}. \quad (64)$$

The space of admissible variations must ensure that $\phi(\tilde{\boldsymbol{\varepsilon}}^p, \tilde{\boldsymbol{\kappa}}, \tilde{\boldsymbol{\varepsilon}}^r, \tilde{\alpha}, \nabla \tilde{\alpha}; \boldsymbol{\kappa}, \alpha, \boldsymbol{\sigma}, \gamma) < +\infty$. In this way, the global dissipative power entering the stability condition (19) remains finite, and we are able to consider the non-trivial conditions for stability. For the sake of conciseness, this requirement has been already embedded in the definition of the function spaces through the constraints. Thus, we set

$$\tilde{\mathbf{q}} \in \tilde{\mathcal{Q}} := \tilde{\mathcal{U}} \times \tilde{\mathcal{B}} \times \cdots \times \tilde{\mathcal{B}} \times \tilde{\mathcal{K}}(\tilde{\boldsymbol{\varepsilon}}_1^p) \times \cdots \times \tilde{\mathcal{K}}(\tilde{\boldsymbol{\varepsilon}}_{n_y}^p) \times \tilde{\mathcal{R}}(\tilde{\boldsymbol{\varepsilon}}^p) \times \tilde{\mathcal{D}}. \quad (65)$$

The governing equations directly follow from enforcing the first-order stability condition (19), the power balance (20) and the dissipation inequality (21). Exploiting the generality of the formulation presented in section 2.3, we directly replace the free energy density (46) and the dissipation potential (53) in the weak form of the first-order stability condition (22) to obtain, for all $\tilde{\mathbf{q}} \in \tilde{\mathcal{Q}}$:

$$\begin{aligned} \int_{\Omega} \left[\sum_{s=1}^{n_y} \left[(\boldsymbol{\sigma} - g(\alpha) H_s^{\text{kin}} \boldsymbol{\varepsilon}_s^p) : \hat{\mathbf{n}}_s - \sqrt{\frac{2}{3}} \left(g(\alpha) (\boldsymbol{\sigma}_s^p + H_s^{\text{iso}} \boldsymbol{\kappa}_s) - \eta_{ps}^2 \text{div} [g(\alpha) \nabla \boldsymbol{\kappa}_s] \right) \right] \|\tilde{\boldsymbol{\varepsilon}}_s^p\| - \left(g'(\alpha) (\psi^{e+} + \psi^p) \right. \right. \\ \left. \left. + g'(\alpha) \sum_{s=1}^{n_y} \sigma_s^p \boldsymbol{\kappa}_s + d(\gamma) w'(\alpha) - \eta_d^2 \text{div} [d(\gamma) \nabla \alpha] \right) \tilde{\alpha} \right] d\mathbf{x} - \int_{\Gamma} \left(d(\gamma) \eta_d^2 \nabla \alpha \tilde{\alpha} + g(\alpha) \sum_{s=1}^{n_y} \eta_{ps}^2 \nabla \boldsymbol{\kappa}_s \tilde{\boldsymbol{\kappa}}_s \right) \cdot \mathbf{n} dS \\ \left. + \int_{\Omega} (\text{div} \boldsymbol{\sigma} + \boldsymbol{\rho} \mathbf{b}) \cdot \tilde{\mathbf{u}} d\mathbf{x} - \int_{\Gamma_N} (\boldsymbol{\sigma} \cdot \mathbf{n} - \bar{\mathbf{t}}) \cdot \tilde{\mathbf{u}} dS \leq 0. \right. \end{aligned} \quad (66)$$

Likewise, using the plastic flow relations (30) and (31), the power balance principle (23) gives

$$\begin{aligned} \int_{\Omega} \left[\sum_{s=1}^{n_y} \left[(\boldsymbol{\sigma} - g(\alpha) H_s^{\text{kin}} \boldsymbol{\varepsilon}_s^p) : \hat{\mathbf{n}}_s - \sqrt{\frac{2}{3}} \left(g(\alpha) (\boldsymbol{\sigma}_s^p + H_s^{\text{iso}} \boldsymbol{\kappa}_s) - \eta_{ps}^2 \text{div} [g(\alpha) \nabla \boldsymbol{\kappa}_s] \right) \right] \|\tilde{\boldsymbol{\varepsilon}}_s^p\| - \left(g'(\alpha) (\psi^{e+} + \psi^p) \right. \right. \\ \left. \left. + g'(\alpha) \sum_{s=1}^{n_y} \sigma_s^p \boldsymbol{\kappa}_s + d(\gamma) w'(\alpha) - \eta_d^2 \text{div} [d(\gamma) \nabla \alpha] \right) \dot{\alpha} \right] d\mathbf{x} - \int_{\Gamma} \left(d(\gamma) \eta_d^2 \nabla \alpha \dot{\alpha} + g(\alpha) \sum_{s=1}^{n_y} \eta_{ps}^2 \nabla \boldsymbol{\kappa}_s \dot{\boldsymbol{\kappa}}_s \right) \cdot \mathbf{n} dS \\ \left. + \int_{\Omega} (\text{div} \boldsymbol{\sigma} + \boldsymbol{\rho} \mathbf{b}) \cdot \dot{\mathbf{u}} d\mathbf{x} - \int_{\Gamma_N} (\boldsymbol{\sigma} \cdot \mathbf{n} - \bar{\mathbf{t}}) \cdot \dot{\mathbf{u}} dS - \int_{\Gamma_D} (\boldsymbol{\sigma} \cdot \mathbf{n} - \mathbf{t}_r) \cdot \dot{\mathbf{u}} dS = 0. \right. \end{aligned} \quad (67)$$

As in section 2.3.2, equations (66) and (67) yield the equilibrium equations and boundary conditions (1), along with equilibrium at the Dirichlet boundary. On the other hand, defining the s^{th} plastic yield function as

$$f_s^p := \|\boldsymbol{\sigma}_{\text{dev}} - g(\alpha) H_s^{\text{kin}} \boldsymbol{\varepsilon}_s^p\| - \sqrt{\frac{2}{3}} \left(g(\alpha) (\boldsymbol{\sigma}_s^p + H_s^{\text{iso}} \boldsymbol{\kappa}_s) - \eta_{ps}^2 \text{div} [g(\alpha) \nabla \boldsymbol{\kappa}_s] \right), \quad (68)$$

and the damage yield function as

$$f^d := -g'(\alpha)(\psi^{e+} + \psi^p) - g'(\alpha) \sum_{s=1}^{n_y} \sigma_s^p \kappa_s - d(\gamma)w'(\alpha) + \eta_d^2 \operatorname{div}[d(\gamma)\nabla\alpha], \quad (69)$$

the evolution equations emerge from equations (66), (67) and the irreversibility condition (45) as loading/unloading systems, along with boundary conditions of the gradient-enhanced variables:

$$\begin{cases} f_s^p \leq 0, & f_s^p \dot{\kappa}_s = 0, & \dot{\kappa}_s \geq 0, \\ \nabla \kappa_s \cdot \mathbf{n} = 0, & \forall s \in Y, \end{cases} \quad \begin{cases} f^d \leq 0, & f^d \dot{\alpha} = 0, & \dot{\alpha} \geq 0, \\ \nabla \alpha \cdot \mathbf{n} = 0. \end{cases} \quad (70)$$

3.4. An overview of the proposed model

Equation (68) can be viewed as a damage-dependent version of the plastic yield function (37). Specifically, the plastic driving force $\|\boldsymbol{\sigma}_{\text{dev}} - g(\alpha)H_s^{\text{kin}}\boldsymbol{\varepsilon}_s^p\|$ is now a function of damage through the stress tensor (51) and the back stress $g(\alpha)H_s^{\text{kin}}\boldsymbol{\varepsilon}_s^p$. Moreover, the size of the yield surface is now given by

$$\sqrt{\frac{2}{3}} \left(g(\alpha)(\sigma_s^p + H_s^{\text{iso}}\kappa_s) - \eta_{ps}^2 \operatorname{div}[g(\alpha)\nabla\kappa_s] \right),$$

which progressively decreases as $\alpha \rightarrow 1$.

In the damage yield function (69), we identify

$$R(\alpha, \nabla\alpha, \gamma) := d(\gamma)w'(\alpha) - \eta_d^2 \operatorname{div}[d(\gamma)\nabla\alpha] \quad (71)$$

as the damage resisting force with fatigue effects. We denote the damage driving force by $D := D^e + D^p$, where D^e and D^p are, respectively, elastic and plastic contributions given by

$$D^e(\boldsymbol{\varepsilon}^e, \alpha) := -g'(\alpha)\psi^{e+} \quad \text{and} \quad D^p(\boldsymbol{\varepsilon}^p, \boldsymbol{\kappa}, \nabla\boldsymbol{\kappa}, \alpha) := -g'(\alpha) \left(\psi^p + \sum_{s=1}^{n_y} \sigma_s^p \kappa_s \right). \quad (72)$$

As in standard phase-field models, the notion of *driving* and *resisting* forces refers to the energetic competition between the damage energy release rate and the critical fracture energy [19]. The main difference is that in the present model, the driving force contains both elastic and plastic contributions, while the resisting force is degraded through the fatigue variable γ . These definitions are useful to describe the mechanical response in the numerical simulations presented in section 4. Equation (69) can be written as

$$f^d = D(\boldsymbol{\varepsilon}^e, \boldsymbol{\varepsilon}^p, \boldsymbol{\kappa}, \nabla\boldsymbol{\kappa}, \alpha) - R(\alpha, \nabla\alpha, \gamma) = D^e(\boldsymbol{\varepsilon}^e, \alpha) + D^p(\boldsymbol{\varepsilon}^p, \boldsymbol{\kappa}, \nabla\boldsymbol{\kappa}, \alpha) - R(\alpha, \nabla\alpha, \gamma). \quad (73)$$

We observe in equation (73) two distinctive fatigue mechanisms:

1. The accumulation of elastic free energy, which, in the absence of plastic strains, drives cracks in the high-cycle fatigue regime. This effect is attained by the multiplicative degradation of the damage resisting force through $d(\gamma)$.
2. The accumulation of plastic energy (free and dissipated), which drives cracks in the low-cycle fatigue regime by additively increasing the damage driving force through D^p . This mechanism entails, on its own, a low-cycle fatigue process, that is accelerated when $d(\gamma) < 1$, where the plastic strains also contribute to the degradation of the damage resisting force (equation (59)). We associate the combination of $D^p > 0$ and $d(\gamma) < 1$ with very-low-cycle fatigue.

3.5. Incremental minimization and numerical implementation

As in section 2.4, consider the time discretization $0 = t_0 < \dots < t_n < t_{n+1} < \dots < t_{n_t} = t_{\max}$, where all quantities are known up to t_n , and the goal is to find the state at the current time step t_{n+1} . For convenience, we introduce the following notations. A quantity \square evaluated at any previous time step $0 \leq i \leq n$ is denoted as \square_i , while a quantity evaluated at t_{n+1} is written without a subscript, i.e., $\square := \square_{n+1}$. Moreover, the operator $\Delta \square := \square - \square_n$ is used to denote an increment from t_n to t_{n+1} .

Recall that the dissipation potential (53) explicitly depends on the stress $\boldsymbol{\sigma}$ and the history variable γ . As a consequence, the dissipated energy is not a state function. In agreement with section 2.4, the dissipated energy increment is evaluated as

$$\begin{aligned} & \int_{\Omega} \int_{t_n}^{t_{n+1}} \left[\sum_{s=1}^{n_y} \left(g(\alpha) \sigma_s^p \dot{\boldsymbol{\kappa}}_s + g'(\alpha) \sigma_s^p \boldsymbol{\kappa}_s \dot{\alpha} + \sqrt{\frac{3}{2}} \beta \|\boldsymbol{\sigma}_{\text{dev}}\| \dot{\boldsymbol{\kappa}}_s \right) + d(\gamma) (w'(\alpha) \dot{\alpha} + \eta_d^2 \nabla \alpha \cdot \nabla \dot{\alpha}) \right] dt d\mathbf{x} \\ &= \int_{\Omega} \int_{t_n}^{t_{n+1}} \underbrace{\left[\sum_{s=1}^{n_y} \left(g(\alpha) \sigma_s^p \dot{\boldsymbol{\kappa}}_s + g'(\alpha) \sigma_s^p \boldsymbol{\kappa}_s \dot{\alpha} \right) \right]}_{\text{path-independent}} + \underbrace{\left[\sqrt{\frac{3}{2}} \beta \|\boldsymbol{\sigma}_{\text{dev}}\| \sum_{s=1}^{n_y} \boldsymbol{\kappa}_s + d(\gamma) \frac{d}{dt} \left(w(\alpha) + \frac{1}{2} \eta_d^2 \nabla \alpha \cdot \nabla \alpha \right) \right]}_{\text{path-dependent}} dt d\mathbf{x}. \end{aligned} \quad (74)$$

Evaluating the path-independent part directly and using the incremental approximation (27) for the path-dependent part, we obtain

$$\mathcal{D}(\boldsymbol{\kappa}_n, \alpha_n, \boldsymbol{\kappa}, \alpha; \boldsymbol{\sigma}_n, \gamma_n) = \int_{\Omega} \left[\sum_{s=1}^{n_y} g(\alpha) \sigma_s^p \boldsymbol{\kappa}_s + \sqrt{\frac{3}{2}} \beta \|\boldsymbol{\sigma}_{\text{dev}n}\| \sum_{s=1}^{n_y} \boldsymbol{\kappa}_s + d(\gamma_n) \left(w(\alpha) + \frac{1}{2} \eta_d^2 \nabla \alpha \cdot \nabla \alpha \right) \right] \Big|_n^{n+1} d\mathbf{x}. \quad (75)$$

In view of equation (28), a time-discrete energy functional is defined as

$$\Pi(\mathbf{u}, \boldsymbol{\varepsilon}^p, \boldsymbol{\kappa}, \boldsymbol{\varepsilon}^r, \alpha) = \mathcal{E}(\mathbf{u}, \boldsymbol{\varepsilon}^p, \boldsymbol{\kappa}, \boldsymbol{\varepsilon}^r, \alpha) - \mathcal{T}(\mathbf{u}_n, \mathbf{u}) + \mathcal{D}(\boldsymbol{\kappa}_n, \alpha_n, \boldsymbol{\kappa}, \alpha; \boldsymbol{\sigma}_n, \gamma_n), \quad (76)$$

such that the incremental minimization problem (28) takes the form

$$\inf_{\{\mathbf{u}, \boldsymbol{\varepsilon}^p, \boldsymbol{\kappa}, \boldsymbol{\varepsilon}^r, \alpha\} \in \mathcal{Q}} \left\{ \Pi(\mathbf{u}, \boldsymbol{\varepsilon}^p, \boldsymbol{\kappa}, \boldsymbol{\varepsilon}^r, \alpha) \mid \Delta \boldsymbol{\kappa}_s = \sqrt{\frac{2}{3}} \|\Delta \boldsymbol{\varepsilon}_s^p\| \forall s \in Y, \Delta \boldsymbol{\varepsilon}^r = \beta \hat{\mathbf{r}}_n \sum_{s=1}^{n_y} \|\Delta \boldsymbol{\varepsilon}_s^p\|, \Delta \alpha \geq 0 \right\}, \quad (77)$$

where we impose irreversibility and the incremental counterparts of the plastic flow relations (30) and (31).

The numerical solution of the variational problem (77) is based on an extension of the alternate minimization algorithm [101] to ductile fracture [30, 37], where the solution of a sequence of convex optimization problems is sought, aiming to iteratively converge to a stationary state. The procedure is summarized in algorithm 1, along with the equations presented below.

Given \mathbf{q}_i for all $i \in \{0, \dots, n\}$, we solve, alternatively, the following coupled sub-problems.

Minimization with respect to the displacement field. Given $\{\boldsymbol{\varepsilon}^p, \boldsymbol{\kappa}, \boldsymbol{\varepsilon}^r, \alpha\}$, find

$$\mathbf{u} = \arg \inf_{\mathbf{u} \in \mathcal{U}} \{ \Pi(\mathbf{u}, \boldsymbol{\varepsilon}^p, \boldsymbol{\kappa}, \boldsymbol{\varepsilon}^r, \alpha) \} \quad (78)$$

from the necessary condition

$$\int_{\Omega} (\boldsymbol{\sigma} : \nabla^s \tilde{\mathbf{u}} - \rho \mathbf{b} \cdot \tilde{\mathbf{u}}) d\mathbf{x} - \int_{\Gamma_N} \bar{\mathbf{t}} \cdot \tilde{\mathbf{u}} dS = 0 \quad \forall \tilde{\mathbf{u}} \in \tilde{\mathcal{U}}. \quad (79)$$

Algorithm 1 Alternate minimization.

Input: $\mathbf{q}_i \in \mathcal{Q}$ for all $i = 0, \dots, n$.

Output: $\mathbf{q}_{n+1} \in \mathcal{Q}$.

1: Initialize iterations $j = 0$ and set $\{\boldsymbol{\varepsilon}^{\text{p}(0)}, \boldsymbol{\kappa}^{(0)}, \boldsymbol{\varepsilon}^{\text{r}(0)}, \alpha^{(0)}\} := \{\boldsymbol{\varepsilon}_n^{\text{p}}, \boldsymbol{\kappa}_n, \boldsymbol{\varepsilon}_n^{\text{r}}, \alpha_n\}$.

2: **repeat**

3: Set $j \leftarrow j + 1$.

4: Find

$$\mathbf{u}^{(j)} := \arg \inf_{\mathbf{u} \in \mathcal{U}} \Pi(\mathbf{u}, \boldsymbol{\varepsilon}^{\text{p}(j-1)}, \boldsymbol{\kappa}^{(j-1)}, \boldsymbol{\varepsilon}^{\text{r}(j-1)}, \alpha^{(j-1)})$$

from equation (79).

5: Find

$$\begin{aligned} \{\boldsymbol{\varepsilon}^{\text{p}(j)}, \boldsymbol{\kappa}^{(j)}, \boldsymbol{\varepsilon}^{\text{r}(j)}\} &:= \arg \inf_{\{\boldsymbol{\varepsilon}^{\text{p}}, \boldsymbol{\kappa}, \boldsymbol{\varepsilon}^{\text{r}}\} \in \mathcal{P}} \{\Pi(\mathbf{u}^{(j)}, \boldsymbol{\varepsilon}^{\text{p}}, \boldsymbol{\kappa}, \boldsymbol{\varepsilon}^{\text{r}}, \alpha^{(j-1)})\} \\ \text{s.t. } \Delta \boldsymbol{\kappa}_s &= \sqrt{\frac{2}{3}} \|\Delta \boldsymbol{\varepsilon}_s^{\text{p}}\| \forall s \in Y, \quad \Delta \boldsymbol{\varepsilon}^{\text{r}} = \beta \hat{\mathbf{r}}_n \sum_{s=1}^{n_y} \|\Delta \boldsymbol{\varepsilon}_s^{\text{p}}\| \end{aligned}$$

from equation (84).

6: Find

$$\alpha^{(j)} = \arg \inf_{\alpha \in \mathcal{D}} \Pi(\mathbf{u}^{(j)}, \boldsymbol{\varepsilon}^{\text{p}(j)}, \boldsymbol{\kappa}^{(j)}, \boldsymbol{\varepsilon}^{\text{r}(j)}, \alpha)$$

from equation (86).

7: **until** $\|\mathbf{u}^j - \mathbf{u}^{j-1}\|$, $\|\boldsymbol{\kappa}^j - \boldsymbol{\kappa}^{j-1}\|$ and $\|\alpha^j - \alpha^{j-1}\|$ are sufficiently small.

8: Set $\mathbf{q}_{n+1} := \mathbf{q}^{(j)}$.

Given that $\mathbf{u} \in \mathcal{U}$, this problem constitutes the weak form of the equilibrium equations (1). This equation is non-linear due to the elastic energy decomposition (49).

Minimization with respect to the plastic fields. Given $\{\mathbf{u}, \alpha\}$, find

$$\begin{aligned} \{\boldsymbol{\varepsilon}^{\text{p}}, \boldsymbol{\kappa}, \boldsymbol{\varepsilon}^{\text{r}}\} &= \arg \inf_{\{\boldsymbol{\varepsilon}^{\text{p}}, \boldsymbol{\kappa}, \boldsymbol{\varepsilon}^{\text{r}}\} \in \mathcal{P}} \{\Pi(\mathbf{u}, \boldsymbol{\varepsilon}^{\text{p}}, \boldsymbol{\kappa}, \boldsymbol{\varepsilon}^{\text{r}}, \alpha)\} \\ \text{s.t. } \Delta \boldsymbol{\kappa}_s &= \sqrt{\frac{2}{3}} \|\Delta \boldsymbol{\varepsilon}_s^{\text{p}}\| \forall s \in Y, \quad \Delta \boldsymbol{\varepsilon}^{\text{r}} = \beta \hat{\mathbf{r}}_n \sum_{s=1}^{n_y} \|\Delta \boldsymbol{\varepsilon}_s^{\text{p}}\|. \end{aligned} \tag{80}$$

For admissible variations $\{\tilde{\boldsymbol{\varepsilon}}_s^{\text{p}}, \tilde{\boldsymbol{\kappa}}_s, \tilde{\boldsymbol{\varepsilon}}^{\text{r}}\} \in \tilde{\mathcal{B}} \times \tilde{\mathcal{H}}(\tilde{\boldsymbol{\varepsilon}}_s^{\text{p}}) \times \tilde{\mathcal{H}}(\tilde{\boldsymbol{\varepsilon}}^{\text{p}})$, it can be shown that the functional derivative of (76) with respect to the plastic variables gives the weak form for the s^{th} yield surface

$$\begin{aligned} \int_{\Omega} \left[\left(-\sqrt{\frac{3}{2}} \|\boldsymbol{\sigma}_{\text{dev}} - g(\alpha) H_s^{\text{kin}} \boldsymbol{\varepsilon}_s^{\text{p}}\| + g(\alpha) (\boldsymbol{\sigma}_s^{\text{p}} + H_s^{\text{iso}} \boldsymbol{\kappa}_s) - \sqrt{\frac{3}{2}} \beta \Delta \boldsymbol{\sigma} : \hat{\mathbf{r}}_n \right) \tilde{\boldsymbol{\kappa}}_s + g(\alpha) \eta_{\text{ps}}^2 \nabla \boldsymbol{\kappa}_s \cdot \nabla \tilde{\boldsymbol{\kappa}}_s \right] d\mathbf{x} \geq 0, \\ \text{with } \boldsymbol{\kappa}_s = \boldsymbol{\kappa}_{sn} + \sqrt{\frac{2}{3}} \|\Delta \boldsymbol{\varepsilon}_s^{\text{p}}\|, \quad \boldsymbol{\varepsilon}^{\text{r}} = \boldsymbol{\varepsilon}_n^{\text{r}} + \beta \hat{\mathbf{r}}_n \sum_{j=1}^{n_y} \|\Delta \boldsymbol{\varepsilon}_j^{\text{p}}\|. \end{aligned} \tag{81}$$

This expression represents the incremental version of the plastic yield function in weak form, from which the continuous equation is recovered by letting the term $\sqrt{3/2} \beta \Delta \boldsymbol{\sigma} : \hat{\mathbf{r}}_n$ vanish for small-enough time steps. To solve equation (81) in a convenient way, we formulate a reduced problem in terms of the scalar field $\boldsymbol{\kappa}_s$. The goal is to express, for each yield surface, the tensor-valued quantities as a function of $\boldsymbol{\kappa}_s$, which is readily

achieved for the ratcheting strain tensor as

$$\boldsymbol{\varepsilon}^r(\boldsymbol{\kappa}) = \boldsymbol{\varepsilon}_n^r + \sqrt{\frac{3}{2}} \beta \hat{\mathbf{n}} \sum_{s=1}^{n_y} \Delta \kappa_s. \quad (82)$$

For the plastic strain tensor, we make use of standard arguments of J_2 plasticity to show that

$$\boldsymbol{\varepsilon}_s^p(\kappa_s) = \boldsymbol{\varepsilon}_{sn}^p + \sqrt{\frac{3}{2}} \hat{\mathbf{n}}_s^{\text{trial}} \Delta \kappa_s \quad \text{with} \quad \hat{\mathbf{n}}_s^{\text{trial}} = \frac{\mathbf{s}_{s \text{ dev}}^{\text{p trial}}}{\|\mathbf{s}_{s \text{ dev}}^{\text{p trial}}\|} \equiv \hat{\mathbf{n}}_s \quad \text{and} \quad \mathbf{s}_{s \text{ dev}}^{\text{p trial}} = \boldsymbol{\sigma}_{s \text{ dev}}^{\text{trial}} - H_s^{\text{kin}} \boldsymbol{\varepsilon}_{sn}^p, \quad (83)$$

where, for the multi-surface ratcheting model, the trial deviatoric stress reads

$$\boldsymbol{\sigma}_{s \text{ dev}}^{\text{trial}}(\boldsymbol{\varepsilon}, \boldsymbol{\varepsilon}_{j \neq s}^p, \boldsymbol{\kappa}, \alpha) = 2g(\alpha) \mu (\boldsymbol{\varepsilon}_{\text{dev}} - (\boldsymbol{\varepsilon}_{sn}^p + \sum_{j \neq s} \boldsymbol{\varepsilon}_j^p) - \boldsymbol{\varepsilon}^r(\boldsymbol{\kappa})).$$

Note that the parametrizations (82) and (83) must be subject to the irreversibility condition $\Delta \kappa_s \geq 0$.

Introducing these results in (81) yields the following non-linear PDE in terms of κ_s :

$$\int_{\Omega} \left[\left(-\sqrt{\frac{3}{2}} \|\mathbf{s}_{s \text{ dev}}^{\text{p trial}}\| + g(\alpha) (\sigma_s^p + H_s^{\text{iso}} \kappa_s + (2\mu + H_s^{\text{kin}}) \Delta \kappa_s) + \partial_{\kappa_s} I_+(\Delta \kappa_s) \right) \tilde{\kappa}_s + g(\alpha) \eta_{\text{ps}}^2 \nabla \kappa_s \cdot \nabla \tilde{\kappa}_s \right] \text{d}\mathbf{x} \ni 0, \quad (84)$$

where the indicator function $I_+ : \mathbb{R} \rightarrow \mathbb{R} \cup \{+\infty\}$ is used to impose irreversibility.

Equation (84) evaluated for all $s \in Y$ yields a system of n_y constrained, non-linear equations with coupled κ_s . This system can be solved iteratively, for instance, using a fixed-point iteration scheme. Then, in each iteration, equation (84) is solved independently for the s^{th} yield surface given the current estimates of $\{\boldsymbol{\varepsilon}_{j \neq s}^p, \kappa_{j \neq s}\}$. Clearly, for the single-surface case, a single non-linear equation must be solved.

Minimization with respect to the damage field. Given $\{\mathbf{u}, \boldsymbol{\varepsilon}^p, \boldsymbol{\kappa}, \boldsymbol{\varepsilon}^r\}$, find

$$\alpha = \arg \inf_{\alpha \in \mathcal{D}} \{ \Pi(\mathbf{u}, \boldsymbol{\varepsilon}^p, \boldsymbol{\kappa}, \boldsymbol{\varepsilon}^r, \alpha) + \int_{\Omega} I_+(\Delta \alpha) \text{d}\mathbf{x} \}. \quad (85)$$

The indicator function is used to impose irreversibility, while the box constraint $\alpha(\mathbf{x}) \in [0, 1]$ in Ω must also be enforced for $\alpha \in \mathcal{D}$ to hold. Equation (85) yields, for all $\tilde{\alpha} \in \tilde{\mathcal{D}}$, the necessary condition

$$\int_{\Omega} \left[\left(g'(\alpha) (\psi^{\text{e}+} + \psi^p) + g'(\alpha) \sum_{s=1}^{n_y} \sigma_s^p \kappa_s + d(\gamma_n) w'(\alpha) + \partial_{\alpha} I_+(\Delta \alpha) \right) \tilde{\alpha} + d(\gamma_n) \eta_{\text{d}}^2 \nabla \alpha \cdot \nabla \tilde{\alpha} \right] \text{d}\mathbf{x} \ni 0, \quad (86)$$

which recovers the damage loading/unloading conditions in equation (70).

Equations (79), (84) and (86) are suitable for spatial discretization using standard finite elements. The non-linearities in the mechanical balance and plasticity equations (79) and (84) are tackled at each alternate minimization iteration with a standard Newton scheme, for which the maximum number of iterations is generally much lower than the required number of alternate minimization iterations at the corresponding time step. On the other hand, the constraints present in the plasticity and damage equations (84) and (86) can be tackled using techniques for PDE-constrained optimization. Examples of such techniques in the context of phase-field fracture modeling are outlined by Gerasimov and De Lorenzis [102]. Herein, we apply a simple algorithmic procedure adopted in previous works [37, 103], where unconstrained equations are first solved and an a posteriori correction is applied to the solution.

4. Numerical simulations

This section presents numerical simulations that highlight the main features of the model described in section 3. In order to highlight the various dissipative mechanisms and their interplay, the homogeneous 1D uniaxial response is first studied. Then, 2D finite element simulations are performed under plane strain conditions. As done for the 1D case, the first 2D simulation addresses the response of the cyclic plasticity model without damage. This example allows to describe a variety of plastic responses with cyclic effects. Then, examples involving fatigue crack growth coupled to cyclic plasticity are presented, capturing the initiation and propagation of ductile fatigue cracks.

4.1. Homogeneous uniaxial response

The aim of this example is to provide an interpretation of the failure mechanisms that result from coupling cyclic plasticity to damage with fatigue effects. For illustrative purposes, we study the response of a single 1D element under either force loading or displacement loading. To this end, consider a straightforward reformulation of the multidimensional model presented in section 3 to the 1D case, where all vector- and tensor-valued quantities are replaced by scalar quantities, and a homogeneous response is assumed. With an obvious change of notation, the plasticity and damage yield functions (68) and (69) become

$$\begin{aligned} f_s^p &= |\sigma - g(\alpha)H_s^{\text{kin}}\varepsilon_s^p| - g(\alpha)(\sigma_s^p + H_s^{\text{iso}}\kappa_s), \\ f^d &= -g'(\alpha)(\psi^e + \psi^p) - g'(\alpha)\sum_{s=1}^{n_y}\sigma_s^p\kappa_s - d(\gamma)w'(\alpha), \end{aligned} \quad (87)$$

where, denoting the Young's modulus by E :

$$\sigma = g(\alpha)E\left(\varepsilon - \sum_{s=1}^{n_y}\varepsilon_s^p - \varepsilon^r\right), \quad \psi^e = \frac{1}{2}E\left(\varepsilon - \sum_{s=1}^{n_y}\varepsilon_s^p - \varepsilon^r\right)^2, \quad \psi^p = \frac{1}{2}\sum_{s=1}^{n_y}(H_s^{\text{iso}}\kappa_s^2 + H_s^{\text{kin}}\varepsilon_s^{p2}). \quad (88)$$

Table 3. Fixed parameters for the homogeneous uniaxial responses, with varying parameters shown in table 4. σ_s^p and H_s^{kin} vary linearly from $s = 1$ to $s = n_y$.

Load type	Model	E [MPa]	w_0 [MPa]	γ_0 [MPa]	k [-]	n_y [-]	σ_1^p [MPa]	$\sigma_{n_y}^p$ [MPa]	H_1^{kin} [MPa]	$H_{n_y}^{\text{kin}}$ [MPa]
Force	AT-2	10	$\infty / 260$	$\infty / 10$	0.4	20	0.6	1.4	100	9.09
Displacement	AT-1	1	$\infty / 750 / 75$	$\infty / 10 / 1$	0.4	10	0.4	0.7	8	0.73

To capture a smooth stress-strain response, the 1D element is modeled with multi-surface plasticity ($n_y > 1$). The parameters shown in tables 3 and 4 are considered to trigger a variety of behaviors, combining the purely kinematic response (KH) with isotropic hardening (KH-IH); isotropic softening (KH-IS); ratcheting (KH-R); isotropic hardening and ratcheting (KH-IH-R); and isotropic softening and ratcheting (KH-IS-R). The loading consists of imposed stress cycles between -0.5 MPa and 1.5 MPa for force loading and imposed strain cycles between -1 and 4 for displacement loading.

Table 4. Varying parameters for the homogeneous uniaxial responses, with fixed parameters shown in table 3. H_s^{kin} varies linearly from $s = 1$ to $s = n_y$, with $n_y = 20$ for force loading and $n_y = 10$ for displacement loading.

Load type	Response	H_1^{iso} [MPa]	$H_{n_y}^{\text{iso}}$ [MPa]	β [-]
Force	KH	0	0	0
	KH-IH	0.2	0.0182	0
	KH-IS	-0.08	-0.0073	0
	KH-R	0	0	0.5
	KH-IH-R	0.2	0.0182	0.5
	KH-IS-R	-0.08	-0.0073	0.5
Displacement	KH	0	0	0
	KH-IH	0.02	0.0018	0
	KH-IS	-0.015	-0.0014	0
	KH-R	0	0	0.2
	KH-IH-R	0.02	0.0018	0.2
	KH-IS-R	-0.015 / -0.075	-0.0014 / -0.0068	0.2

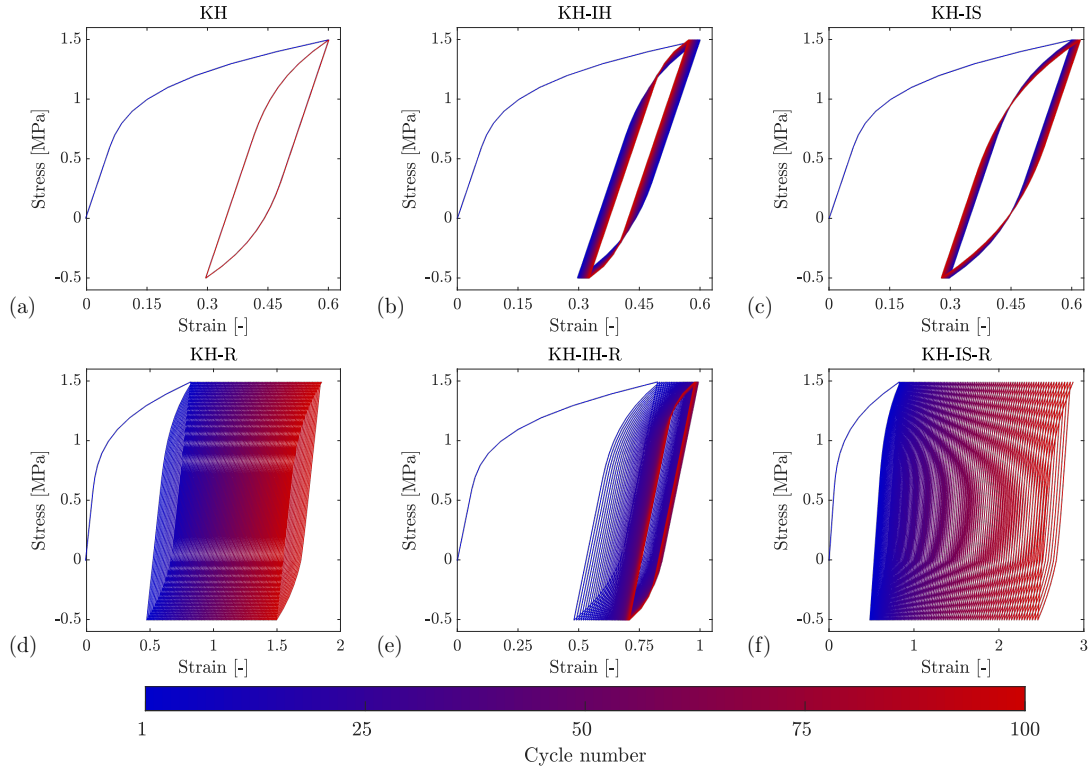


Fig. 1. Stress-strain curves of the homogeneous uniaxial tests under force loading, showing the undamaged response for (a) KH, (b) KH-IH, (c) KH-IS, (d) KH-R, (e) KH-IH-R and (f) KH-IS-R.

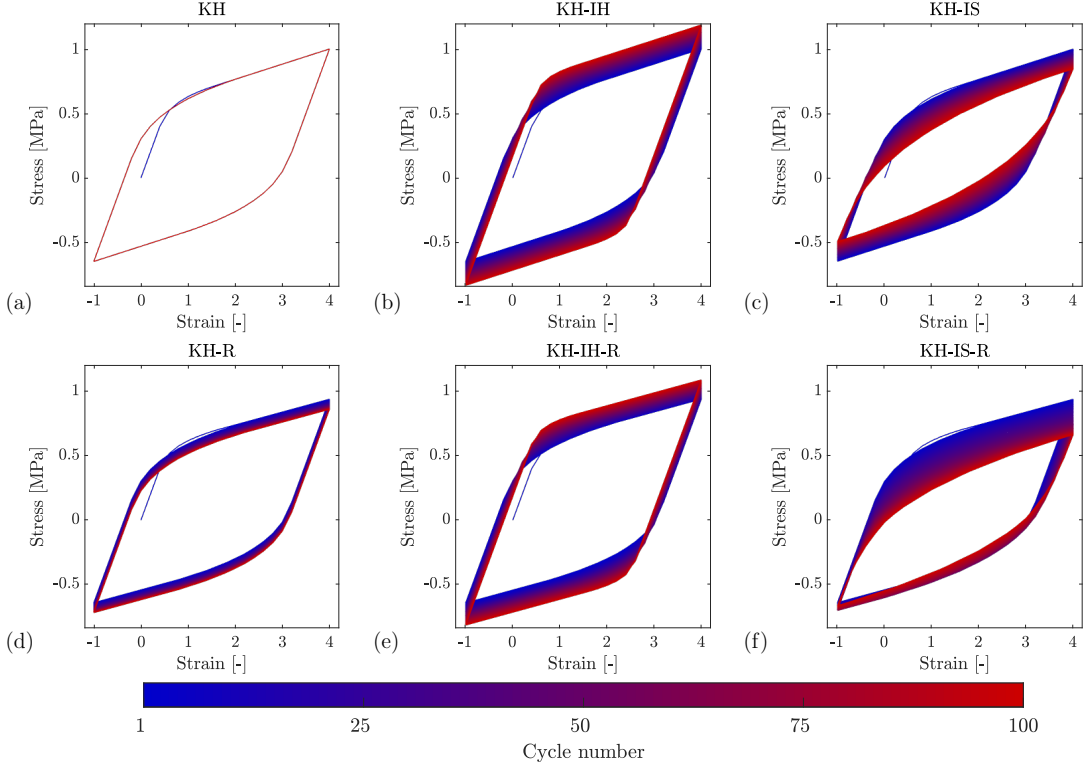


Fig. 2. Stress-strain curves of the homogeneous uniaxial tests under displacement loading, showing the undamaged response for (a) KH, (b) KH-IH, (c) KH-IS, (d) KH-R, (e) KH-IH-R and (f) KH-IS-R.

Figure 1 shows the undamaged responses under force loading, ensured by setting $w_0 = \infty$ and $\gamma_0 = \infty$. The KH response exhibits closed hysteresis loops, while including isotropic hardening (KH-IH) results in a progressive decrease in cyclic strain amplitude. The opposite occurs with isotropic softening (KH-IS), where the cyclic strain amplitude progressively increases as the size of the yield surface decreases. The combination of these responses with ratcheting effects results in more complex cyclic evolutions. KH-R exhibits mean cyclic strain increments at a constant rate, i.e., a purely ratcheting response. Combining ratcheting with isotropic hardening (KH-IH-R) results in a competition between both mechanisms, where the ratcheting effect tends to vanish as the equivalent plastic strains increase. As a result of the loading pattern, this response occurs asymmetrically, with more pronounced cyclic hardening during tensile loading. On the other hand, KH-IS-R leads to an asymmetric accelerated ratcheting response.

Figure 2 shows the undamaged responses under displacement loading. As under force loading conditions, a closed cycle is observed for KH, while the yield surface progressively grows for KH-IH, leading to an elastic response after a sufficiently large number of cycles. The opposite occurs for KH-IS, where the size of the yield surface progressively decreases. In both KH-IH and KH-IS, the response is symmetric in tension and compression. On the other hand, for $\beta > 0$ (non-zero ratcheting strains), the response becomes asymmetric. This interesting effect of the ratcheting model allows to capture stress relaxation, as shown in figure 2(d) for KH-R, where the plastic cycles shift downwards. Moreover, an asymmetrical response is observed for

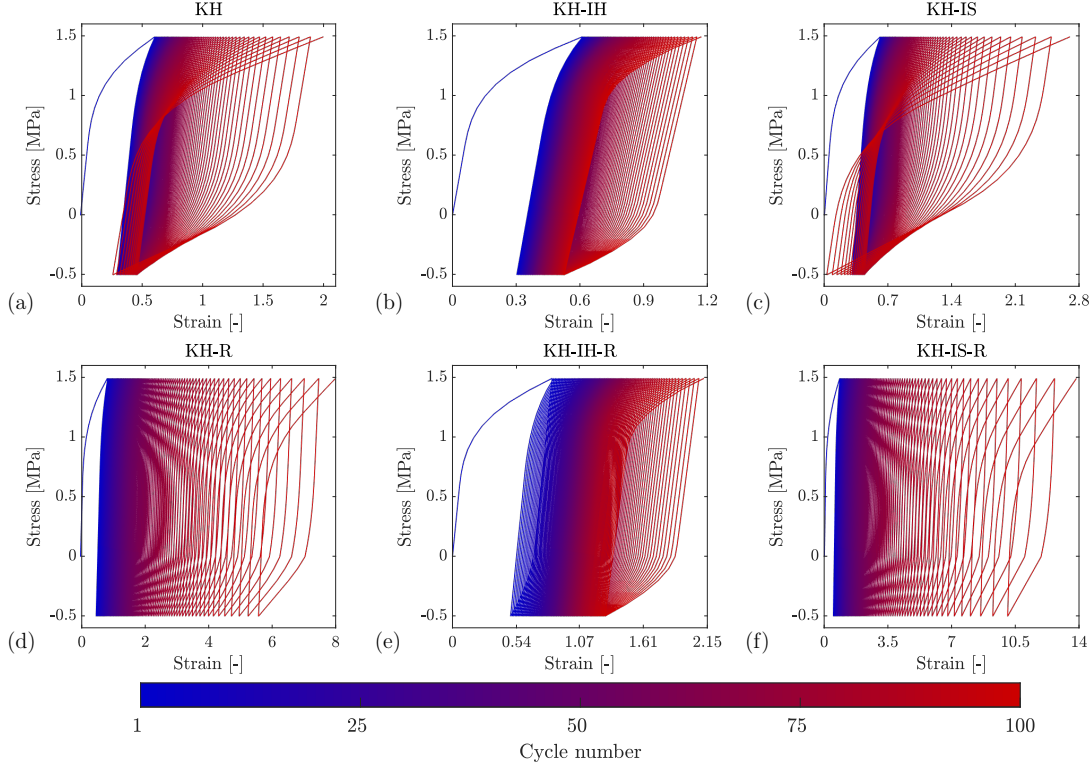


Fig. 3. Stress-strain curves of the homogeneous uniaxial tests under force loading, showing (a) KH, (b) KH-IH, (c) KH-IS, (d) KH-R, (e) KH-IH-R and (f) KH-IS-R coupled to damage with fatigue effects.

both KH-IH-R and KH-IS-R, which combine stress relaxation with cyclic hardening and cyclic softening, respectively. For KH-IS-R, we have set $H_1^{\text{iso}} = -0.015$ MPa and $H_{n_v}^{\text{iso}} = -0.0014$ MPa (table 4).

The result of coupling these responses to damage evolution is shown in figure 3 for force loading, obtained by setting $w_0 = 260$ MPa and $\gamma_0 = 10$ MPa (table 3). In this case, the initial plastic responses resemble the results in figure 1. However, as damage evolves, cyclic softening is triggered in all cases. Therefore, the softening responses are accelerated, while the (initially) hardening responses shift to a cyclic softening regime. An analogous result is observed in figure 4 for the case of displacement loading with $w_0 = 750$ MPa and $\gamma_0 = 10$ MPa.

As previously discussed, the coupled plastic-damage model includes a fatigue mechanism that degrades the damage resisting force through $d(\gamma)$ as a function of free energy accumulation. Thus, in the absence of plastic strains, damage is accelerated for the AT-2 model and triggered after an initial elastic response for the AT-1 model, leading to a high-cycle fatigue process. Responses of this type are thoroughly studied in references [12] and [13]. On the other hand, the accumulation of plastic strains leads, on its own, to a plastic fatigue mechanism that promotes damage evolution through the plastic driving force D^P . We associate this process with low-cycle fatigue, and the combination of D^P and $d(\gamma)$ with very-low-cycle fatigue.

The fatigue mechanisms and their interplay are analyzed in figures 5 to 8 for KH-IS-R. Figure 5 shows the mechanical response for the force loading test with the parameters from tables 3 and 4, this time setting

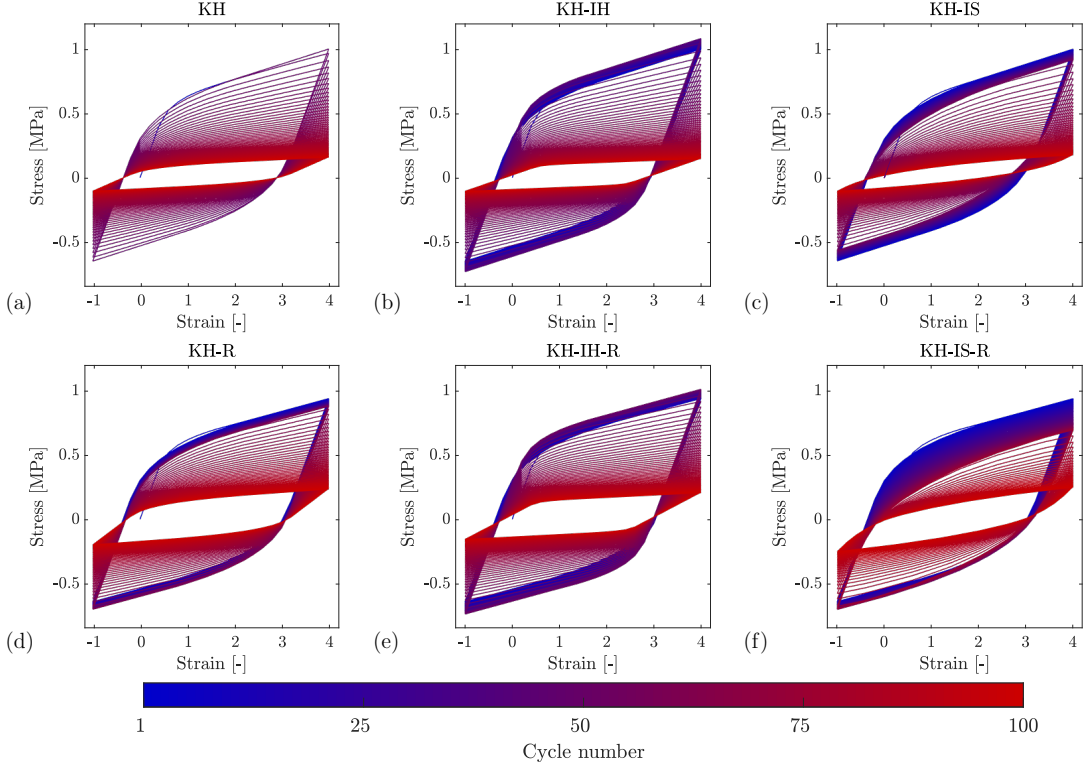


Fig. 4. Stress-strain curves of the homogeneous uniaxial tests under displacement loading, showing (a) KH, (b) KH-IH, (c) KH-IS, (d) KH-R, (e) KH-IH-R and (f) KH-IS-R coupled to damage with fatigue effects.

$\gamma_0 = \infty$, such that damage is only driven by the accumulation of plastic strains. The ratcheting strain ε^r grows in an accelerated manner, where the mean cyclic value progressively increases, while the plastic strains ε_s^p grow in amplitude. These responses are reflected in the cyclic evolution of the total strain ε . As a result of the AT-2 model, the damage resisting force $R = 2w_0\alpha$ shown in figure 5(d) grows as damage evolves. This occurs at every loading stage, where the resisting force intersects the total driving force D . Figure 6 shows the counterpart simulation with $\gamma_0 = 10$ MPa. The ratcheting strain, the total strain and the plastic strains present the same evolution pattern, but grow at a notably higher rate. This is a consequence of the accelerated growth of the damage variable that occurs as $d(\gamma)$ decreases. This response results from the combined effect of D^p and $d(\gamma)$, where the fatigue variable γ is driven by the sum of elastic free energy and plastic free energy.

For the case of displacement loading (figures 7 and 8), we take the values from tables 3 and 4 as $w_0 = 75$ MPa, $H_1^{\text{iso}} = -0.075$ MPa and $H_{n_y}^{\text{iso}} = -0.0068$ MPa, in order to accelerate the softening response for illustrative purposes. We then set, alternatively, $\gamma_0 = \infty$ and $\gamma_0 = 1$ MPa. Figure 7 shows the mechanical response of the displacement loading test with $\gamma_0 = \infty$, exhibiting a relatively slow stress decay. As a result of the AT-1 model, damage is triggered after 12 cycles. This occurs when the total driving force D , modulated by the plastic driving force D^p , intersects the constant-valued resisting force R . Figure 8 shows the counterpart with $\gamma_0 = 1$ MPa, where the resisting force begins to decrease after 2 cycles, causing damage

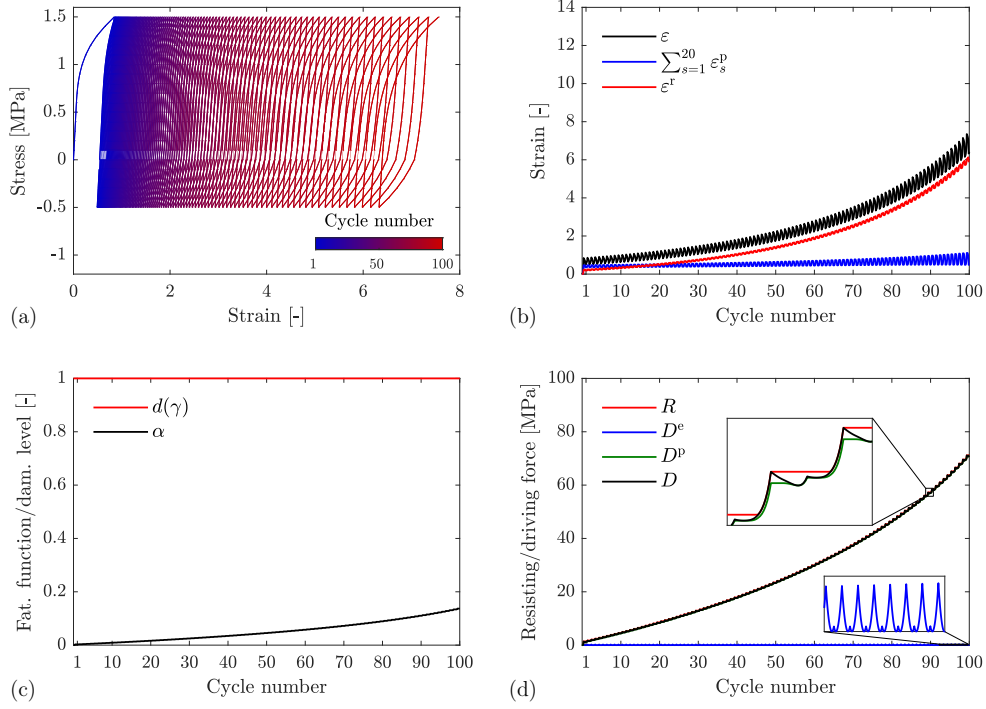


Fig. 5. KH-IS-R homogeneous response with damage ($\gamma_0 = \infty$) under force loading: (a) stress-strain curve and corresponding time histories for the (b) strains, (c) damage and fatigue degradation and (d) damage driving and resisting forces.

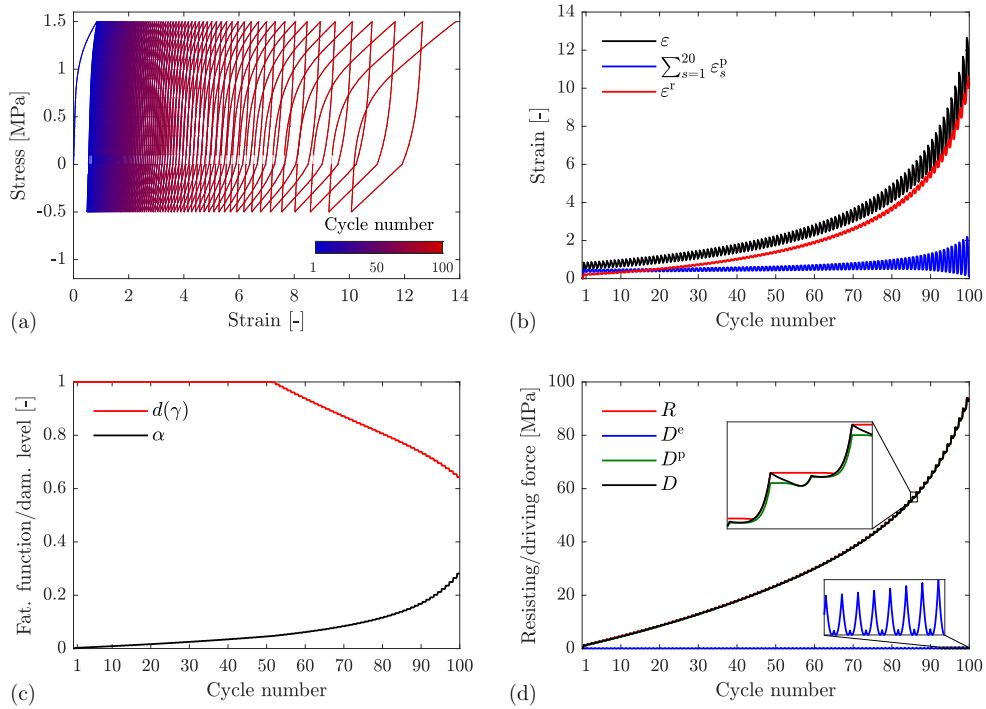


Fig. 6. KH-IS-R homogeneous response with damage ($\gamma_0 = 10$ MPa) under force loading: (a) stress-strain curve and corresponding time histories for the (b) strains, (c) damage and fatigue degradation and (d) damage driving and resisting forces.

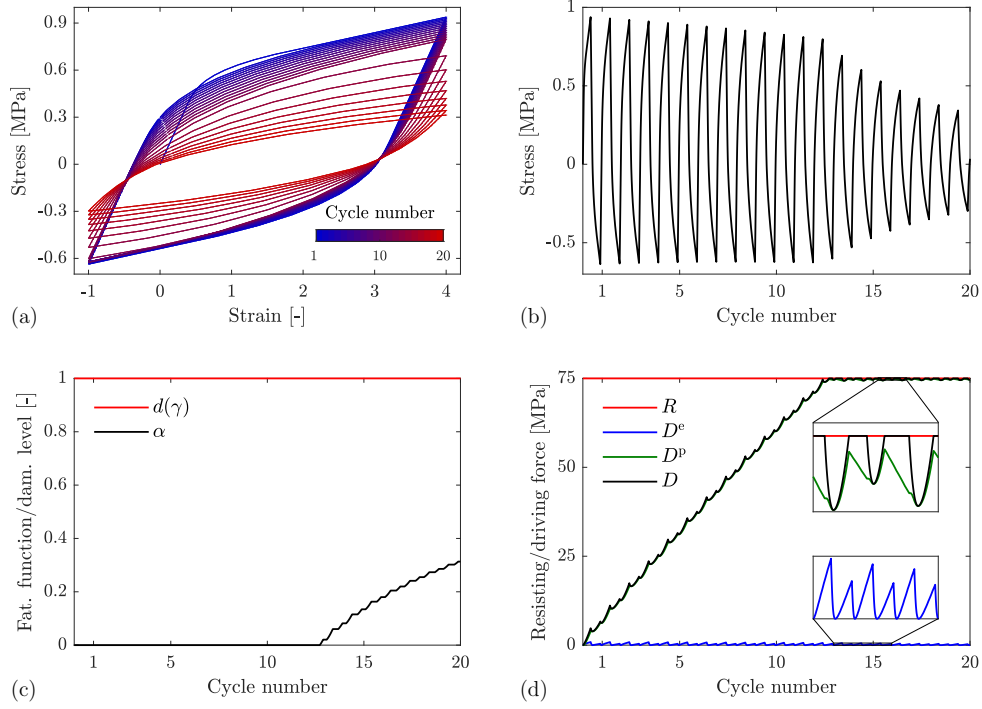


Fig. 7. KH-IS-R homogeneous response with damage ($\gamma_0 = \infty$) under displacement loading: (a) stress-strain curve and corresponding time histories for the (b) stress, (c) damage and fatigue degradation and (d) damage driving and resisting forces.

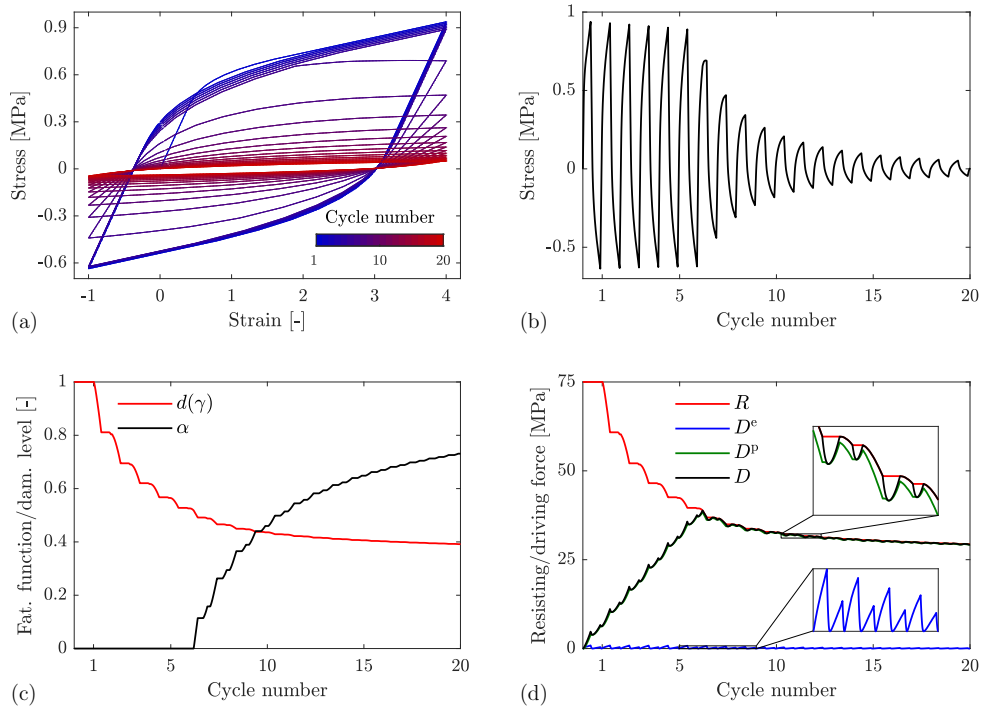


Fig. 8. KH-IS-R homogeneous response with damage ($\gamma_0 = 1$ MPa) under displacement loading: (a) stress-strain curve and corresponding time histories for the (b) stress, (c) damage and fatigue degradation and (d) damage driving and resisting forces.

to be triggered after only 6 cycles (figures 8(c) and 8(d)). Consequently, figure 8(b) shows a notably faster stress decay than figure 7(b), as expected in very-low-cycle fatigue.

4.2. Non-homogeneous finite element simulations

In this subsection, we present a series of 2D simulations under plane strain conditions that highlight the versatility of the proposed model. For simplicity, and to alleviate computational cost, we consider in all examples the case of single-surface plasticity, which is easily recovered from the model presented in section 3 by letting $n_y = 1$. For notational simplicity, the subscripts are thus dropped from the plasticity parameters, such that the isotropic hardening modulus, the kinematic hardening modulus, the yield strength and the characteristic length read H^{iso} , H^{kin} , σ^{p} and ℓ_{p} (alternatively η_{p}), respectively.

In all computations, bilinear quadrilateral elements are employed. The use of C^0 continuous elements is feasible in the present model due to the gradient regularization employed for both plasticity and damage.

4.2.1. Undamaged perforated specimen

This example consists of a square specimen with a central hole under plane strain conditions and cyclic loading, alternatively subjected to force loading and displacement loading. Due to symmetry conditions, only the top-right quarter of the specimen is analyzed (figure 9), and uniform loading is applied on the top border. Unless stated otherwise, a uniform mesh of 800 elements is considered in the simulations, with 120 (160) time steps per cycle for force (displacement) loading.

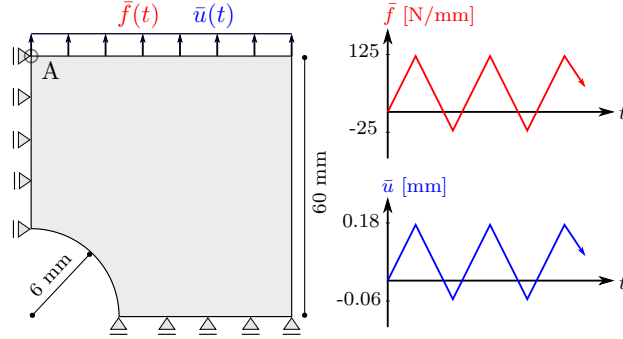


Fig. 9. Schematic representation of the perforated specimen under force loading and displacement loading.

Damage is disallowed by setting, in the general model, a sufficiently large w_0 . We consider a Young's modulus $E = 205 \times 10^3$ MPa, a Poisson's ratio $\nu = 0.3$, a plastic yield strength $\sigma^{\text{p}} = 100$ MPa and an internal length scale $\eta_{\text{p}} = 0.6 \text{ N}^{1/2}$. It is worth mentioning that the effect of the non-local term modulated by η_{p} has little effect for the stress hardening responses of this example. The remaining parameters vary according to table 5, where the kinematic hardening modulus is combined with a positive (negative) isotropic hardening modulus to describe cyclic hardening (softening). Moreover, ratcheting and stress relaxation effects are attained by setting $\beta > 0$.

Table 5. Varying parameters for the cyclically plastic responses of the perforated specimen.

Load type	Response	H^{kin} [MPa]	H^{iso} [MPa]	β [-]
Force	KH	16513.89	0	0
	KH-IH	16348.75	165.14	0
	KH-IS	16447.83	-66.06	0
	KH-R	16513.89	0	0.075
	KH-IH-R	16348.75	165.14	0.1
	KH-IS-R	16447.83	-66.06	0.1
Displacement	KH	16513.89	0	0
	KH-IH	16500.68	13.21	0
	KH-IS	16500.68	-13.21	0
	KH-R	16513.89	0	0.4
	KH-IH-R	16500.68	13.21	0.8
	KH-IS-R	16500.68	-13.21	0.8

Figure 10 shows the cyclic responses under force loading, corresponding to the force-displacement curves in the vertical direction (with displacements measured at location A) due to a uniform distributed force of magnitude $\bar{f}(t)$ (figure 9). The results resemble and further highlight the behaviors presented for the homogeneous uniaxial case: the KH response exhibits closed hysteresis cycles, capturing the Bauschinger effect; KH-IH results in a progressive decrease in cyclic displacements, leading to a closed plastic loop; and KH-IS leads to a progressive increase in cyclic displacements as the size of the yield surface decreases. Likewise, KH-R exhibits ratcheting at a constant rate; KH-IH-R results in a vanishing ratcheting response (i.e., a *shakedown* response) occurring asymmetrically in tension and compression; and KH-IS-R results in an asymmetric accelerated ratcheting response. The last two responses are further observed in figure 11, which shows the time history of the displacements at location A for KH-IH-R and KH-IS-R. The results are shown for different mesh densities, indicating mesh-objectivity.

Figure 12 shows the equivalent plastic strains at different load cycles for KH-IS-R, while the contour plots for the other responses are not shown due to their qualitative similarity. The plastic strains concentrate near the hole and propagate in an inclined pattern, as expected for deviatoric-driven plasticity.

Figure 13 shows the cyclic responses under displacement loading of magnitude $\bar{u}(t)$ applied on the top border (figure 9). As for the case of force loading, the results resemble and further highlight the behaviors presented for the homogeneous uniaxial case, with a closed cycle observed for KH; a progressively growing yield surface for KH-IH; and a progressively vanishing yield surface for KH-IS. Likewise, including ratcheting effects leads to stress relaxation for KH-R, and pronounced asymmetric responses for KH-IH-R and KH-IS-R with cyclic hardening and cyclic softening, respectively. Figure 14 shows the equivalent plastic strains at different load cycles for KH-IS-R, which qualitatively resemble the results obtained under force loading. The

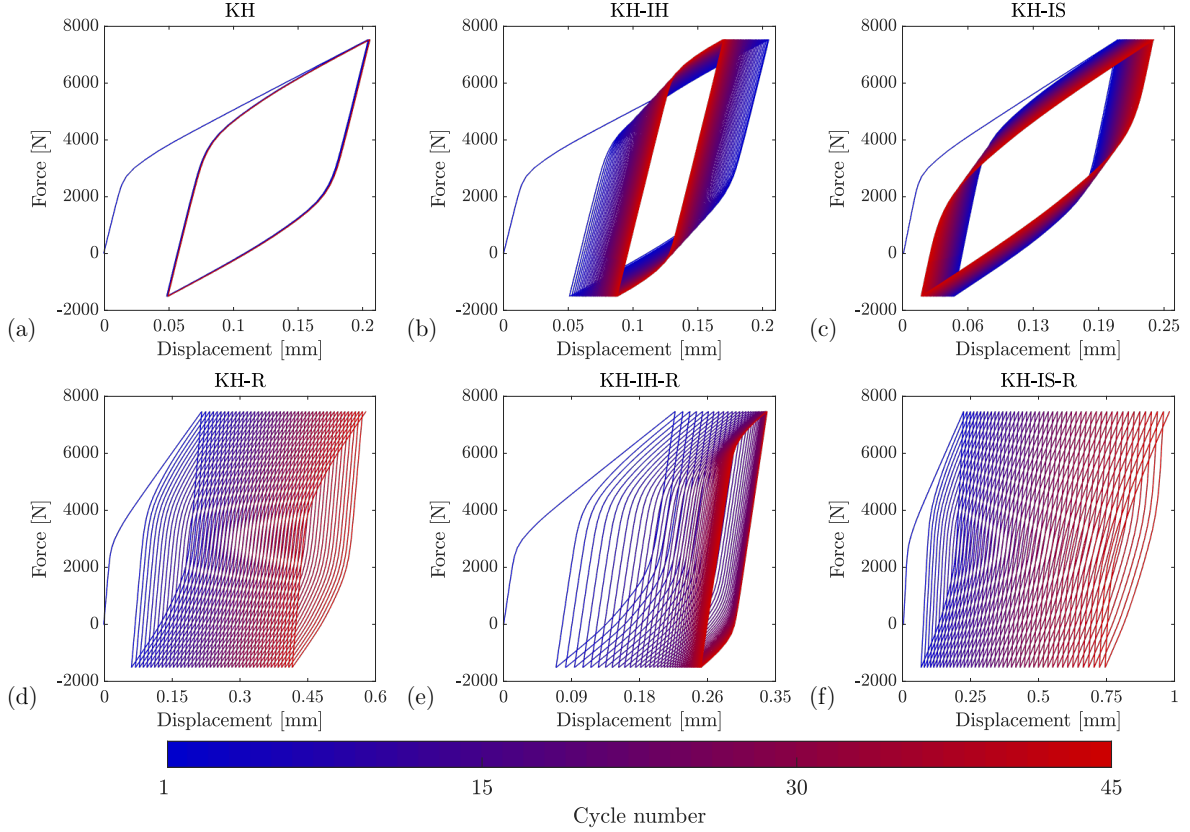


Fig. 10. Force-displacement curves measured at location A of the perforated specimen under force loading (figure 9), showing the cyclic response with (a) KH, (b) KI-IH, (c) KH-IS, (d) KH-R, (e) KH-IH-R and (f) KH-IS-R.

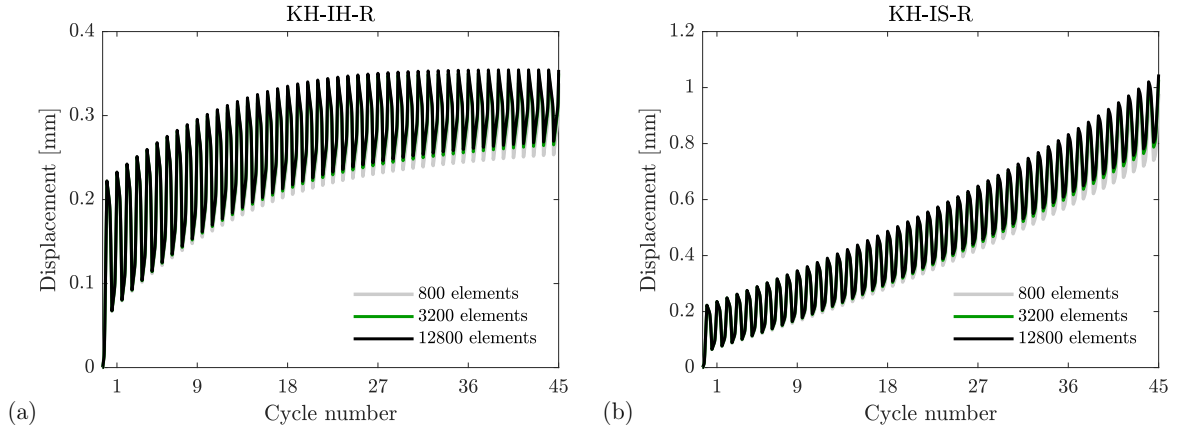


Fig. 11. Time history of the displacement at location A for the perforated specimen under force loading (figure 9) computed with different mesh densities, showing (a) the KH-IH-R response and (b) the KH-IS-R response.

simulation was computed with 800, 3200 and 12800 elements. The results indicate similar mesh convergence as for the case of force loading and are thus not shown for brevity.

From this study, we conclude that the plastic responses observed in figures 10 and 13 encompass a wide

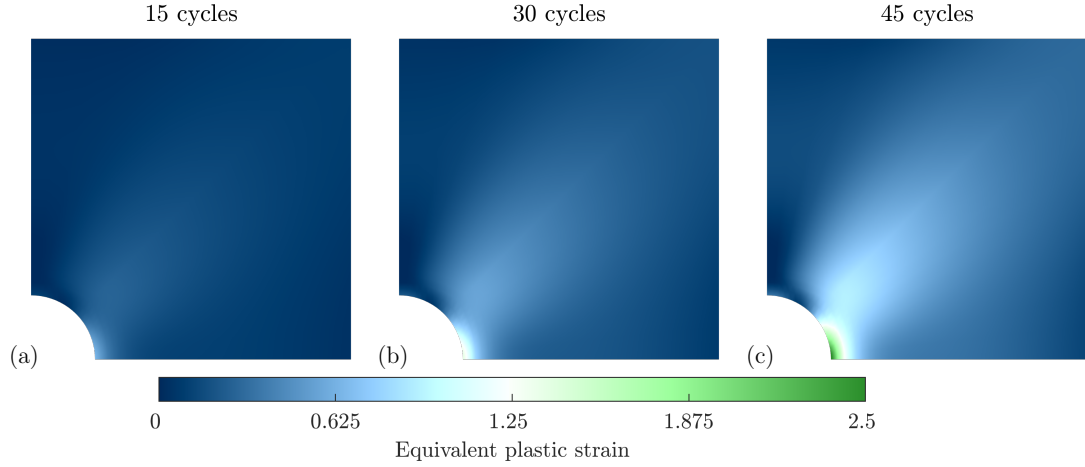


Fig. 12. Equivalent plastic strain for the KH-IS-R response of the perforated specimen under force loading after (a) 15, (b) 30 and (c) 45 cycles.

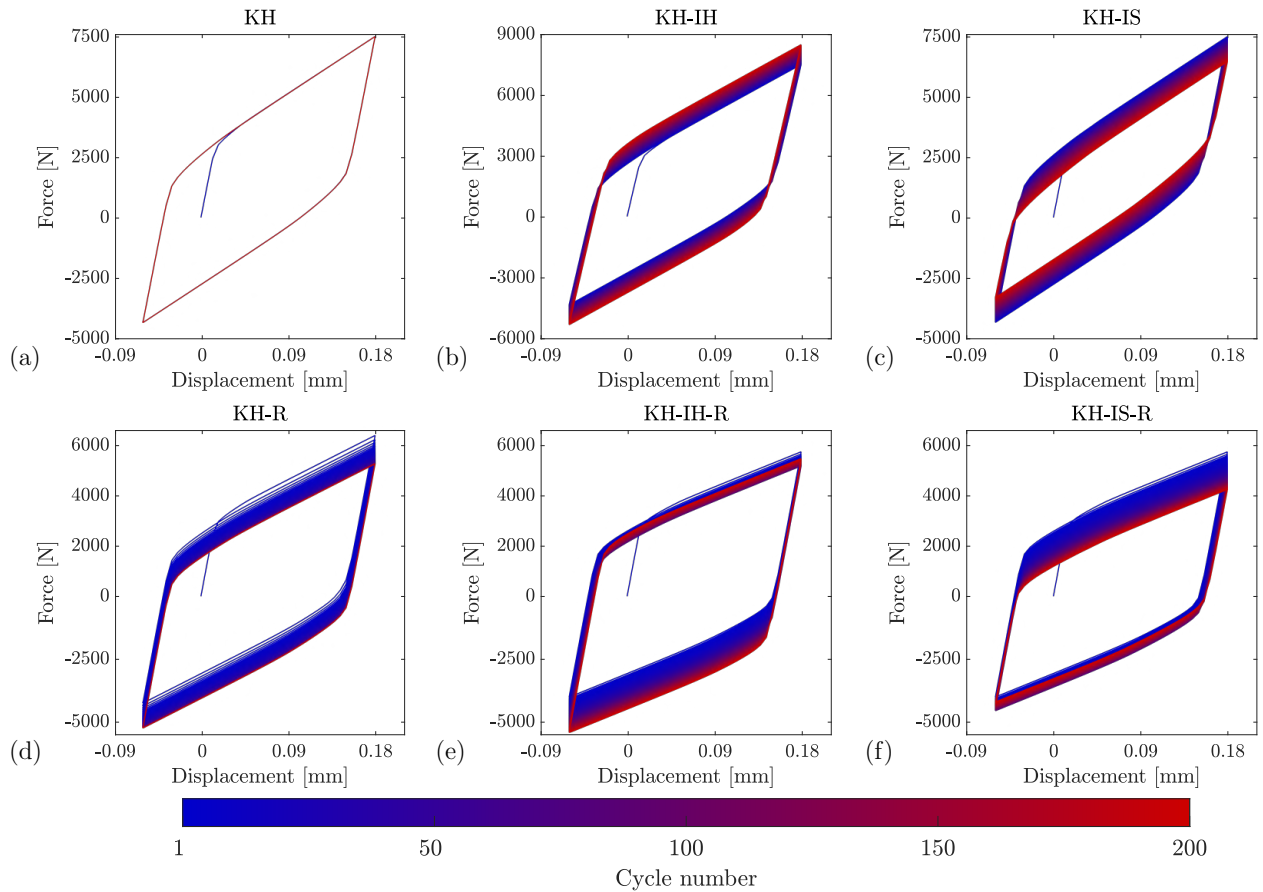


Fig. 13. Force-displacement curves measured at the top border of the perforated specimen under displacement loading (figure 9), showing the cyclic response with (a) KH, (b) KH-IH, (c) KH-IS, (d) KH-R, (e) KH-IH-R and (f) KH-IS-R.

range of material responses in a specimen with geometrical effects or imperfections. Of particular interest

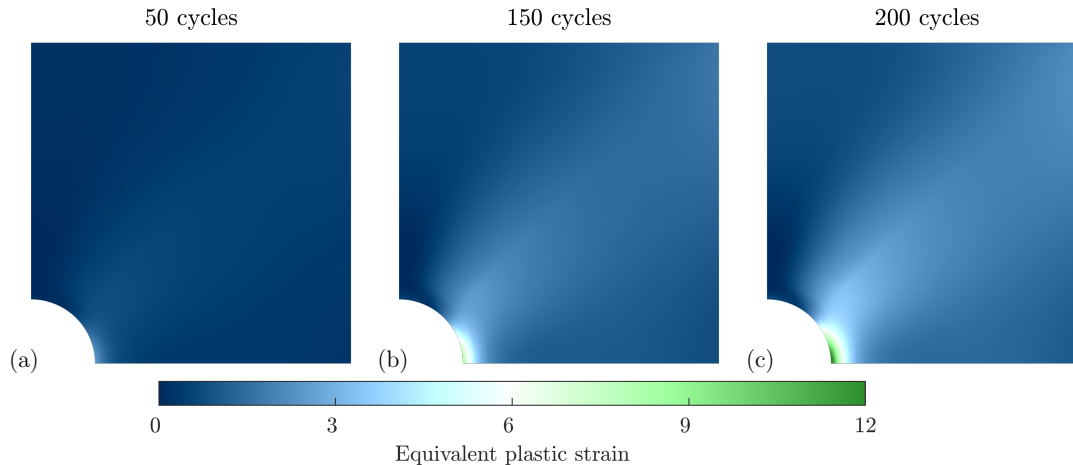


Fig. 14. Equivalent plastic strain for the KH-IS-R response of the perforated specimen under displacement loading after (a) 50, (b) 150 and (c) 200 cycles.

are the responses exhibiting ratcheting and stress relaxation, which are further enriched by including cyclic hardening or cyclic softening effects. This allows to recover complex cyclic behaviors often observed in experimental works [3, 4].

4.2.2. Asymmetrically notched specimen

This example aims to describe the initiation, growth and merging of ductile cracks in a low-cycle fatigue process, driven by the accumulation and localization of isochoric plastic deformations. For this purpose, we subject an asymmetrically notched specimen in plane strain conditions to displacement cycles, as schematically shown in figure 15, where the bottom border is fixed and vertical displacements of magnitude $\bar{u}(t)$ are imposed on the top border, with 300 time steps per cycle.

Table 6. Material parameters for the asymmetrically notched specimen under cyclic loading.

K	ν	w_0	ℓ_d	γ_0	k	σ^P	H^{iso}	H^{kin}	ℓ_p	β
[MPa]	[-]	[MPa]	[mm]	[MPa]	[-]	[MPa]	[MPa]	[MPa]	[mm]	[-]
71659.46	0.331	1428.3	0.2	300	0.4	345	112.5	1591.67	0.25	0.4

Consider the parameters shown in table 6 and the AT-1 damage model (equation (56)). For the numerical simulations, an unstructured mesh of bilinear quadrilateral elements was employed, with local refinement in the region where the crack is expected to develop. In this region, a characteristic element size $h_{\min} \in \{0.16, 0.08, 0.053, 0.04\}$ mm was chosen, aiming for a compromise between (i) a sufficiently large ratio ℓ_d/h_{\min} required to properly describe the phase-field fracture process [18, 104] and (ii) the computational cost associated with the present cyclic simulations. In addition, note from table 6 that, in agreement with Miehe et al. [36], the characteristic length scales have been chosen such that $\ell_p > \ell_d > h_{\min}$, aiming for an objective and physically meaningful description of the coupled plasticity-damage evolution.

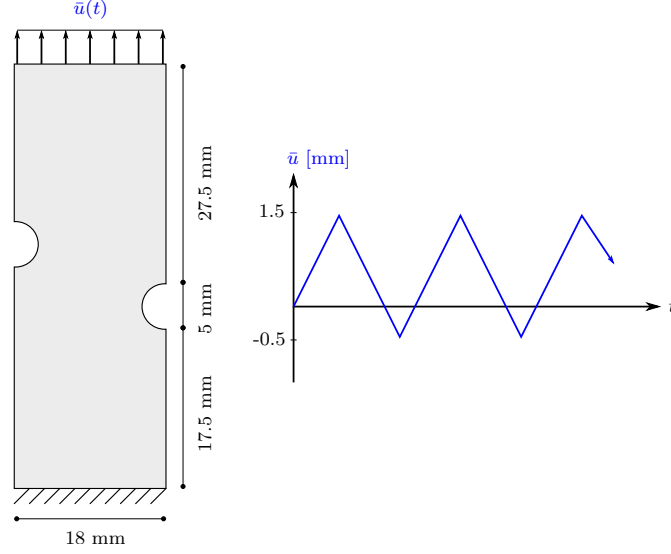


Fig. 15. Schematic representation of the asymmetrically notched specimen under displacement loading.

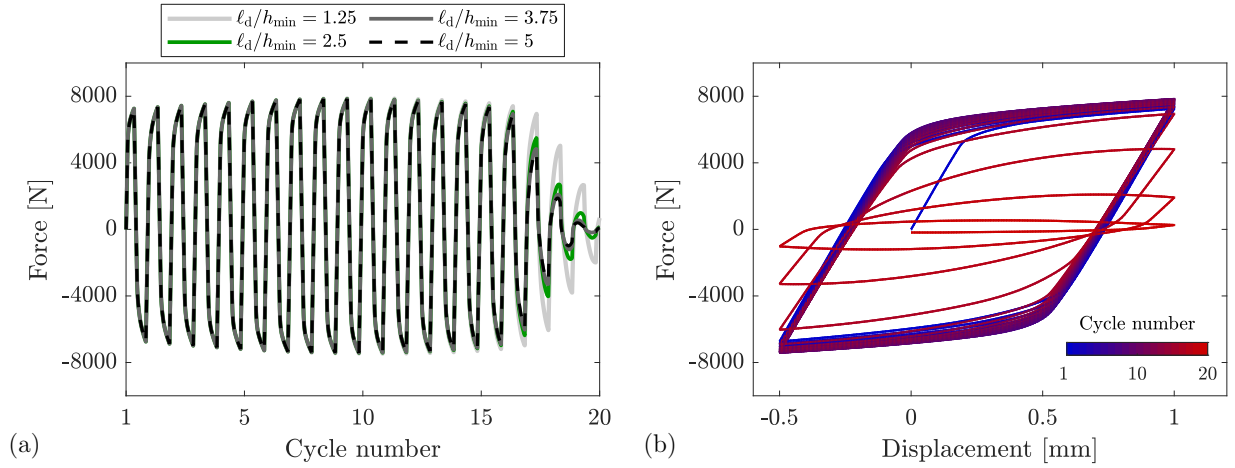


Fig. 16. Results of the asymmetrically notched specimen showing (a) the time history of the reaction force for different mesh sizes and (b) the force-displacement curve for $h_{\min} = 0.053$ mm.

Figure 16(a) shows the time history of the reaction force for the different mesh sizes, where mesh-objective results are observed as h_{\min} decreases with fixed characteristic lengths ℓ_p and ℓ_d . Figure 16(b) shows the force-displacement response measured at the top border of the specimen. Similar to the homogeneous uniaxial response, we observe that the initial hardening loops progressively decrease in amplitude as damage evolves, with the global stiffness vanishing after 20 cycles.

Figure 17 shows contour plots for the equivalent plastic strains and the phase-field/damage variable at different loading stages. After 9 cycles, the plastic strains are localized in relatively wide bands, governed by the plastic length scale. Within these regions, damage is triggered and begins to evolve. After about 15 cycles, individual cracks initiate and propagate from the notches, resulting in a strong localization of

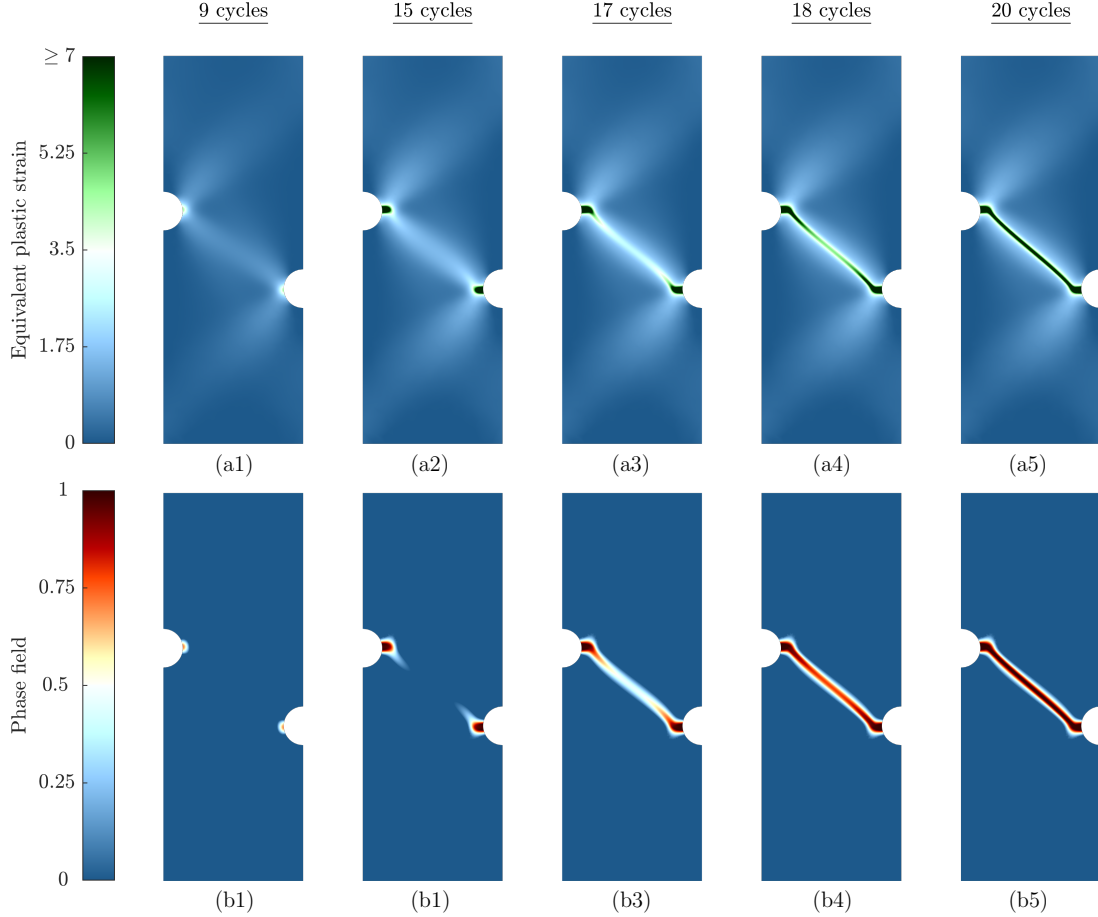


Fig. 17. Equivalent plastic strains (a1)-(a5) and phase field (b1)-(b5) during damage initiation (9 cycles), crack initiation (15 cycles), crack propagation (17-18 cycles), and final merging and fracture stage (20 cycles).

plastic strains. At this stage, the diffuse nature of the plastic strains in the pre-cracked states shifts to a strongly localized evolution, thus capturing the behavior of ductile cracks. At subsequent stages, the cracks propagate and finally merge along a central shear band, leading to a slip-like failure mode after 20 cycles.

In the context of the phase-field approach to ductile fracture, similar examples have been studied under monotonic loading [32, 33, 38]. In particular, Rodríguez et al. [38] present different responses that depend on the degree of ductility: a mixed Mode I/II failure associated with an elastoplastic brittle response, and a Mode II-dominated failure associated with a ductile response. In the present study, the cyclic response is strongly driven by plastic strains and therefore resembles the ductile failure mode obtained for monotonic loading by Rodríguez et al. [38].

An important feature of the proposed model is the non-local treatment of the localized responses for both plasticity and damage, governed by two length scale parameters ℓ_p and ℓ_d . As discussed by Miehe et al. [36] for monotonic fracture, the use of gradient plasticity in phase-field models overcomes mesh-sensitivity in the post-critical stage and avoids unrealistic localization patterns observed in the local plasticity counterpart. This behavior is embedded in the present model, as shown in figure 18 for varying mesh sizes, where the

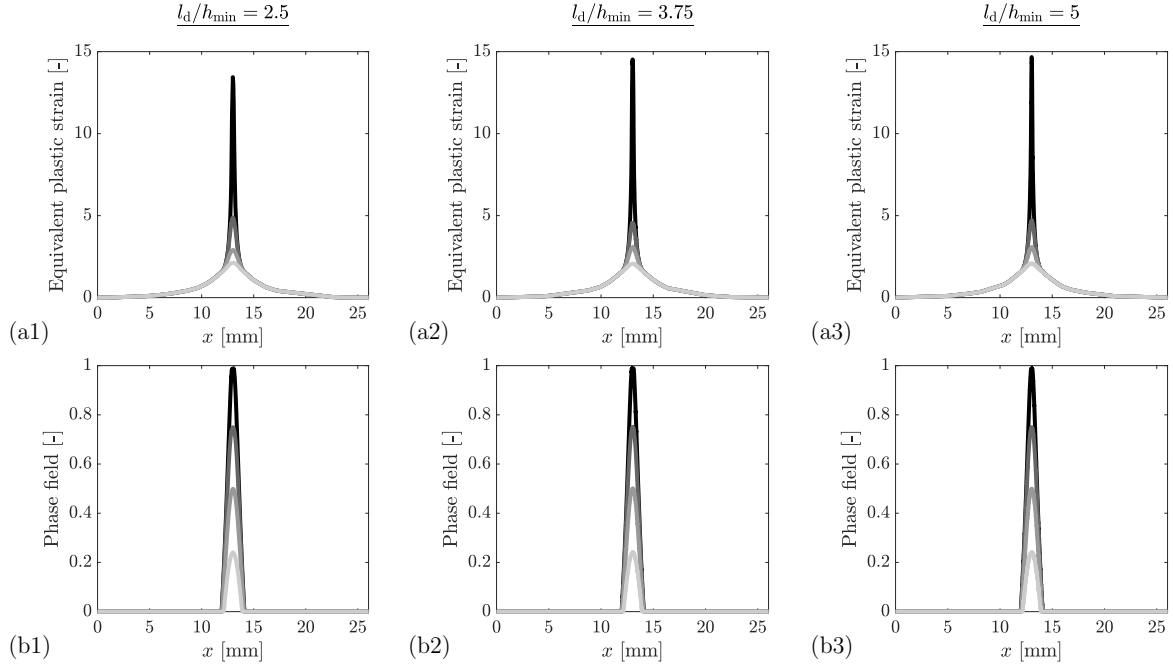


Fig. 18. Equivalent plastic strain (a1)-(a3) and damage (b1)-(b3) profiles for different mesh sizes, showing mesh-objective results for both plasticity and damage. The results are shown when the maximum damage level reaches 0.25 (light gray), 0.5 (medium gray), 0.75 (dark gray) and 0.99 (black). The curves are plotted along a direction orthogonal to the crack in the center of the specimen, where x denotes the distance along the cross-section.

profiles of the equivalent plastic strains and the phase-field variable are plotted along a direction orthogonal to the crack in the center of the specimen.

4.2.3. Compact-tension test

The final example considers a typical fatigue test consisting of a compact-tension specimen subjected to force loading. Figure 19 shows the geometry and loading conditions adopted for the simulations. For the sake of simplicity, as in Seiler et al. [43], a simplified test set-up is considered, where forces are applied on the left-most edges of the specimen as uniformly distributed loads. The load is discretized in 100 time steps per cycle.

Consider the parameters shown in table 7 and the AT-2 damage model (equation (56)). For the numerical simulations, an unstructured mesh of bilinear quadrilateral elements is employed, with local mesh refinement along the direction of the initial crack with a characteristic element size $h_{\min} = 0.13$ mm.

Table 7. Material parameters for the compact-tension specimen under cyclic loading.

K	ν	w_0	ℓ_d	γ_0	k	σ^P	H^{iso}	H^{kin}	ℓ_p	β
[MPa]	[-]	[MPa]	[mm]	[MPa]	[-]	[MPa]	[MPa]	[MPa]	[mm]	[-]
175000	0.3	45.23	0.25	500	0.4	125 / 480 / 720	0	36500	0.75	0.1

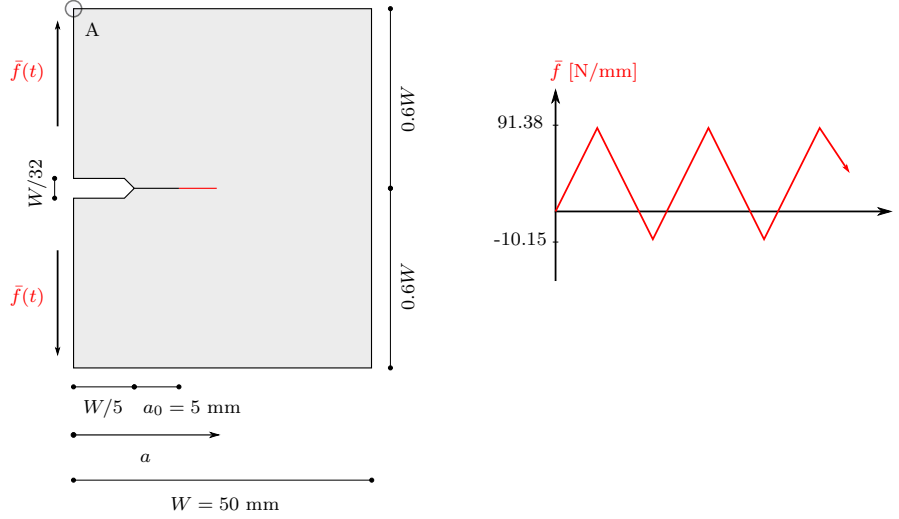


Fig. 19. Schematic representation of the simplified compact-tension specimen with an initial crack of 5 mm under force loading.

In this example, we focus on the influence of ductility in the fatigue fracture process. Consequently, the simulation is computed with different values for the plastic yield strength σ^P . Due to the loading conditions, forces are applied either until the initial crack length is increased to achieve a total length $a \approx 21.5$ mm (figure 19), or until the maximum allowable force is reached at a given time step due to the damage/fatigue-induced cyclic softening response.

The resulting force-displacement curves are shown in figure 20, along with the cyclic crack-growth curves. Figure 20(a) shows a ductile response, exhibiting considerable ratcheting effects. As observed in the homogeneous responses in section 4.1, the ratcheting rate progressively grows as damage evolves and, in particular, as the crack propagates. The simulation ends after 37 cycles, where the maximum allowable force is reached, and the crack has achieved a total length $a = 19.12$ mm. A markedly less ductile response is observed as σ^P increases, with the plastic loops exhibiting very limited ratcheting. The low accumulation of plastic strains thus delays the crack propagation process and allows the specimen to withstand much more cycles prior to attaining a maximum allowable force. For $\sigma^P = 480$ MPa, a total length $a = 21.49$ mm is achieved after 76 cycles, while for $\sigma^P = 720$ MPa, a total length $a = 21.37$ mm is achieved after 200 cycles.

Figure 21 shows the result of continuing the simulation after the cyclic force-loading stage for $\sigma^P = 125$ MPa, where monotonic displacements are imposed after the maximum allowable force has been reached. The contour plot shows the phase-field variable with a relatively large damage region around the crack tip during the cyclic loading process. This is followed first by an instant of brutal crack propagation and then by a stable propagation stage, where a narrow crack is observed to grow as displacements are monotonically imposed.

Figure 22 shows contour plots for the equivalent plastic strains and the phase-field/damage variable for the different yield strengths. As the response becomes less ductile, a markedly smaller plastic region is observed, resulting in a smaller damage zone around the crack tip.

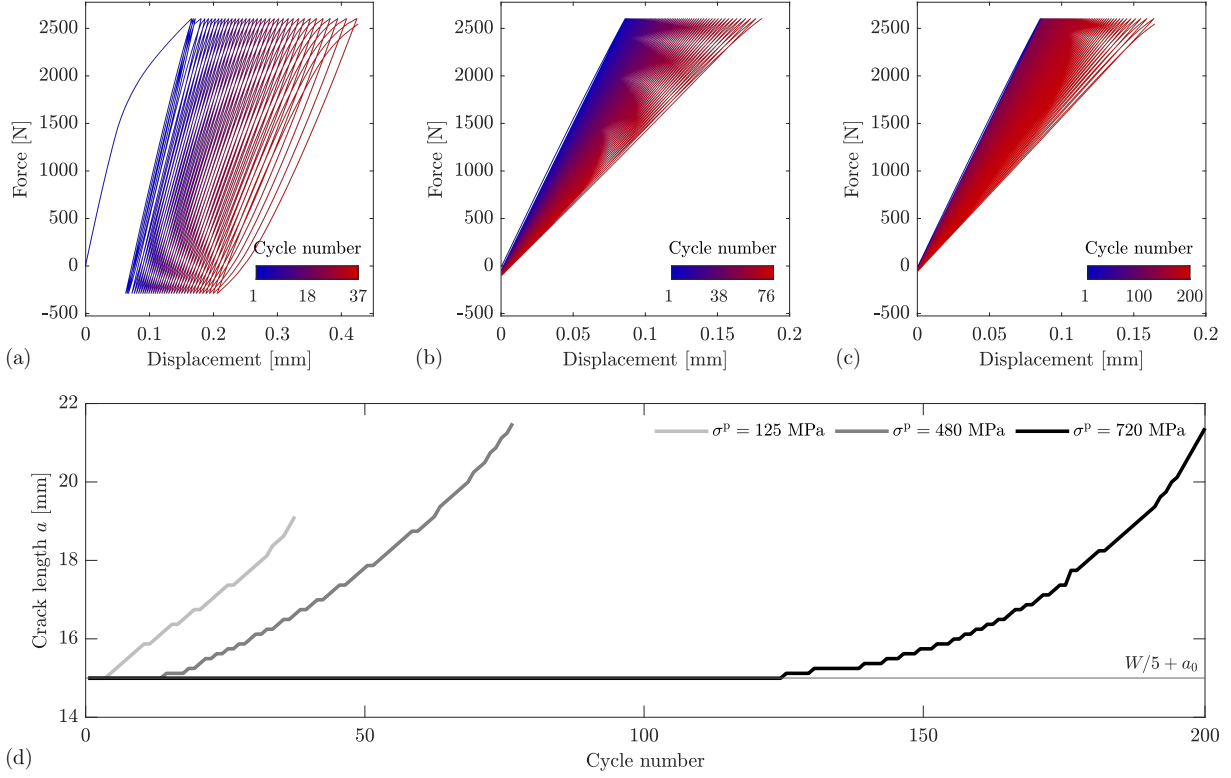


Fig. 20. Force-displacement curves at the top border (displacements at location A; figure 19) for (a) $\sigma^P = 125$ MPa, (b) $\sigma^P = 480$ MPa and (c) $\sigma^P = 720$ MPa. The cyclic crack growth for the three cases is shown in (d).

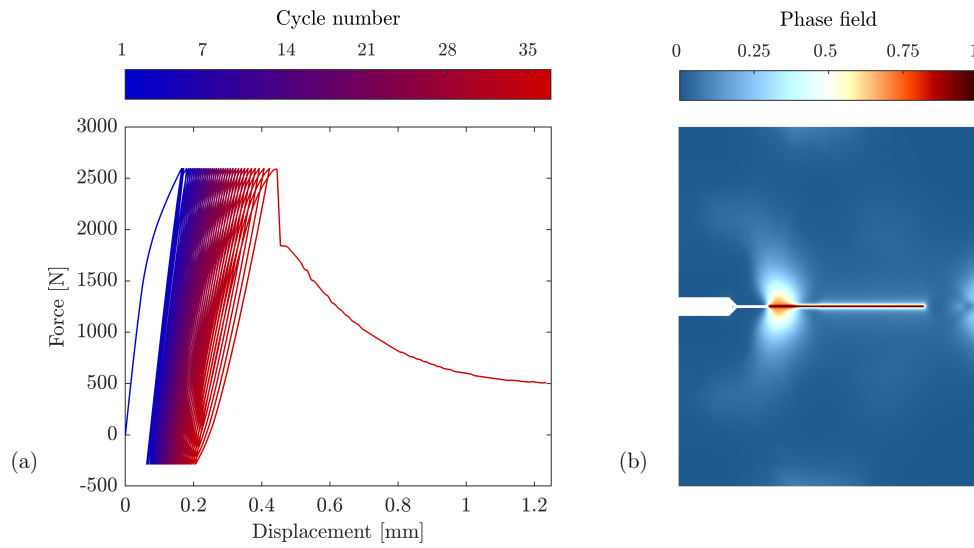


Fig. 21. (a) Force-displacement curve measured at the top border (displacements at location A; figure 19) and (b) phase-field contour plot for $\sigma^P = 125$ MPa. The initial cyclic force-loading stage is followed by monotonically imposed displacements.

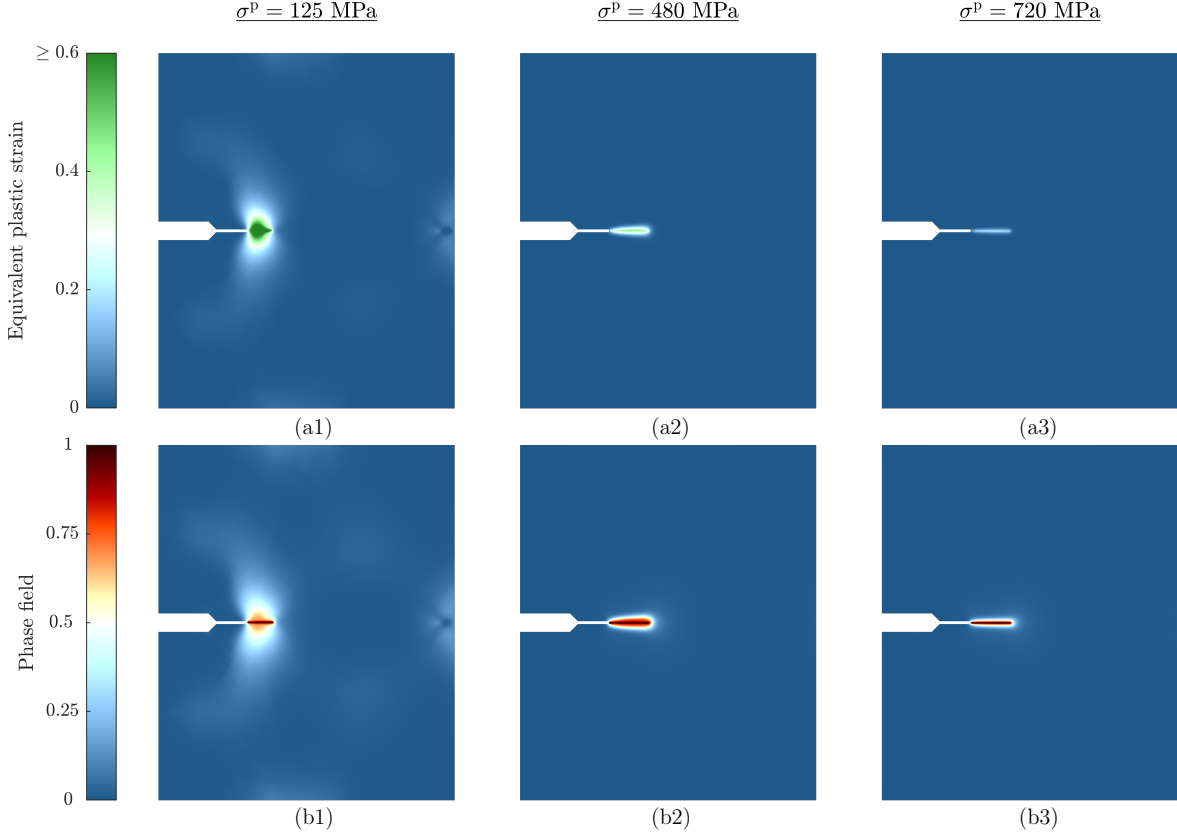


Fig. 22. Equivalent plastic strains (a1)-(a3) and phase field (b1)-(b3) for different yield strengths.

5. Conclusions

In the context of the energetic formulation, we have presented a coupled gradient-enhanced plasticity-damage model that embeds, in a unified way, characteristic features of low- and high-cycle fatigue. The proposed variational model is able to account for cyclic failure under both force and displacement loading by combining a phase-field description of fatigue cracks with cyclic plasticity, including multi-surface kinematic hardening, isotropic hardening/softening and ratcheting. The multi-field governing equations are derived from the principles of the energetic formulation, leading to a robust numerical implementation based on an alternate minimization scheme.

The results of numerical simulations indicate that several material responses can be captured by the cyclic plasticity model, including cyclic hardening and cyclic softening effects, as well as ratcheting under force loading and stress relaxation under displacement loading. Once damage coupling is introduced, the plastic energy accumulation entails a plastic fatigue effect, associated with the low-cycle fatigue regime. The model is further enriched by a fatigue degradation function that is driven by free energy accumulation and degrades the damage resisting force. In the absence of plastic strains, this feature accounts for brittle fracture processes under high-cycle fatigue. The combination of elastic and plastic fatigue mechanisms conceived in an energetic framework allows for a physically sound description of a broad range of behaviors. These results

are evidenced in the study of homogeneous uniaxial responses. Moreover, the results of numerical simulations in a 2D setting highlight the ability of the model to objectively describe fatigue-induced ductile fracture, including the initiation, propagation and merging of ductile cracks.

The present study lays the groundwork for future theoretical developments and a broad range of applications. In addition to the most evident applications in civil and mechanical engineering, the modeling of cyclic inelastic behavior is relevant in a variety of fields ranging from geomechanics [105–107] to electromechanics, e.g., to account for plastic deformations in electrode materials [108, 109], and biomechanics [110, 111], where plastic deformations are observed in biological tissues [112–114]. Concerning the proposed model, quantitative comparisons with experimental results are crucial to calibrate the various mechanisms included in the model and to assess their predictive ability. On the other hand, from a numerical perspective, the development of efficient techniques are of major interest to handle the computational cost of cyclic loading.

Acknowledgements

R. Alessi acknowledges the Italian Ministry of Education, University and Research (MIUR) under the PRIN 2017 20177TTP3S grant.

References

- [1] R.I. Stephens, A. Fatemi, R.R. Stephens, and H.O. Fuchs. *Metal fatigue in engineering*. John Wiley & Sons, 2000.
- [2] J. Lemaitre. *A course on damage mechanics*, volume 2. Springer Berlin, 1996.
- [3] T. Hassan and S. Kyriakides. Ratcheting of cyclically hardening and softening materials: I. uniaxial behavior. *International Journal of Plasticity*, 10(2):149–184, 1994.
- [4] T. Hassan and S. Kyriakides. Ratcheting of cyclically hardening and softening materials: II. multiaxial behavior. *International Journal of Plasticity*, 10(2):185–212, 1994.
- [5] J.L. Chaboche. A review of some plasticity and viscoplasticity constitutive theories. *International Journal of Plasticity*, 24(10):1642–1693, 2008.
- [6] S.K. Paul, S. Sivaprasad, S. Dhar, and S. Tarafder. Cyclic plastic deformation and cyclic hardening/softening behavior in 304ln stainless steel. *Theoretical and Applied Fracture Mechanics*, 54(1):63–70, 2010.
- [7] O.H. Basquin. The exponential law of endurance tests. *Proceedings American Society for Testing Materials*, 10:625–630, 1910.
- [8] P.C. Paris and F. Erdogan. A critical analysis of crack propagation laws. *Journal of Basic Engineering*, 85(4):528–533, 1963.
- [9] R.G. Forman, V.E. Kearney, and R.M. Engle. Numerical analysis of crack propagation in cyclic-loaded structures. *Journal of Basic Engineering*, 89(3):459–463, 1967.
- [10] J. Maierhofer, R. Pippan, and H.P. Gänser. Modified NASGRO equation for physically short cracks. *International Journal of Fatigue*, 59:200–207, 2014.
- [11] R. Desmorat. Damage and fatigue: continuum damage mechanics modeling for fatigue of materials and structures. *Revue Européenne de Génie Civil*, 10(6-7):849–877, 2006.
- [12] R. Alessi, S. Vidoli, and L. De Lorenzis. A phenomenological approach to fatigue with a variational phase-field model: The one-dimensional case. *Engineering Fracture Mechanics*, 190:53–73, 2018.
- [13] P. Carrara, M. Ambati, R. Alessi, and L. De Lorenzis. A framework to model the fatigue behavior of brittle materials based on a variational phase-field approach. *Computer Methods in Applied Mechanics and Engineering*, 361:112731, 2020.
- [14] G.A. Maugin. Internal variables and dissipative structures. *Journal of Non-Equilibrium Thermodynamics*, 15(2):173–192, 1990.
- [15] C. Miehe. A multi-field incremental variational framework for gradient-extended standard dissipative solids. *Journal of the Mechanics and Physics of Solids*, 59(4):898–923, 2011.

- [16] G. Francfort and J.J. Marigo. Revisiting brittle fracture as an energy minimization problem. *Journal of the Mechanics and Physics of Solids*, 46(8):1319–1342, 1998.
- [17] B. Bourdin, G. Francfort, and J.J. Marigo. Numerical experiments in revisited brittle fracture. *Journal of the Mechanics and Physics of Solids*, 48(4):797–826, 2000.
- [18] B. Bourdin, G. Francfort, and J.J. Marigo. The variational approach to fracture. *Journal of Elasticity*, 91(1-3): 5–148, 2008.
- [19] C. Miehe, M. Hofacker, and F. Welschinger. A phase field model for rate-independent crack propagation: Robust algorithmic implementation based on operator splits. *Computer Methods in Applied Mechanics and Engineering*, 199(45):2765–2778, 2010.
- [20] M.J. Borden, C.V. Verhoosel, M.A. Scott, T.J.R. Hughes, and C.M. Landis. A phase-field description of dynamic brittle fracture. *Computer Methods in Applied Mechanics and Engineering*, 217:77–95, 2012.
- [21] M. Ambati, T. Gerasimov, and L. De Lorenzis. A review on phase-field models of brittle fracture and a new fast hybrid formulation. *Computational Mechanics*, 55(2):383–405, 2015.
- [22] K. Pham, H. Amor, J.J. Marigo, and C. Maurini. Gradient damage models and their use to approximate brittle fracture. *International Journal of Damage Mechanics*, 20(4):618–652, 2011.
- [23] K. Pham, J.J. Marigo, and C. Maurini. The issues of the uniqueness and the stability of the homogeneous response in uniaxial tests with gradient damage models. *Journal of the Mechanics and Physics of Solids*, 59(6):1163–1190, 2011.
- [24] J.J. Marigo, C. Maurini, and K. Pham. An overview of the modelling of fracture by gradient damage models. *Meccanica*, 51(12):3107–3128, 2016.
- [25] R. de Borst and C.V. Verhoosel. Gradient damage vs phase-field approaches for fracture: Similarities and differences. *Computer Methods in Applied Mechanics and Engineering*, 312:78–94, 2016.
- [26] N. Moës, J. Dolbow, and T. Belytschko. A finite element method for crack growth without remeshing. *International Journal for Numerical Methods in Engineering*, 46(1):131–150, 1999.
- [27] N. Moës and T. Belytschko. Extended finite element method for cohesive crack growth. *Engineering Fracture Mechanics*, 69(7):813–833, 2002.
- [28] E. Samaniego and T. Belytschko. Continuum–discontinuum modelling of shear bands. *International Journal for Numerical Methods in Engineering*, 62(13):1857–1872, 2005.
- [29] J.Y. Wu, V.P. Nguyen, C.T. Nguyen, D. Sutula, S. Bordas, and S. Sinaie. Phase field modeling of fracture. *Advances in Applied Mechanics: Multi-scale Theory and Computation*, 52, 2018.
- [30] R. Alessi, J.J. Marigo, and S. Vidoli. Gradient damage models coupled with plasticity: variational formulation and main properties. *Mechanics of Materials*, 80:351–367, 2015.

- [31] R. Alessi, J.J. Marigo, C. Maurini, and S. Vidoli. Coupling damage and plasticity for a phase-field regularisation of brittle, cohesive and ductile fracture: one-dimensional examples. *International Journal of Mechanical Sciences*, 149:559–576, 2018.
- [32] F.P. Duda, A. Ciarbonetti, P.J. Sánchez, and A.E. Huespe. A phase-field/gradient damage model for brittle fracture in elastic–plastic solids. *International Journal of Plasticity*, 65:269–296, 2015.
- [33] M. Ambati, T. Gerasimov, and L. De Lorenzis. Phase-field modeling of ductile fracture. *Computational Mechanics*, 55(5):1017–1040, 2015.
- [34] M.J. Borden, T.J.R. Hughes, C.M. Landis, A. Anvari, and I.J. Lee. A phase-field formulation for fracture in ductile materials: Finite deformation balance law derivation, plastic degradation, and stress triaxiality effects. *Computer Methods in Applied Mechanics and Engineering*, 312:130–166, 2016.
- [35] C. Kuhn, T. Noll, and R. Müller. On phase field modeling of ductile fracture. *GAMM-Mitteilungen*, 39(1):35–54, 2016.
- [36] C. Miehe, F. Aldakheel, and S. Teichtmeister. Phase-field modeling of ductile fracture at finite strains: A robust variational-based numerical implementation of a gradient-extended theory by micromorphic regularization. *International Journal for Numerical Methods in Engineering*, 111(9):816–863, 2017.
- [37] J. Ulloa, P. Rodríguez, and E. Samaniego. On the modeling of dissipative mechanisms in a ductile softening bar. *Journal of Mechanics of Materials and Structures*, 11(4):463–490, 2016.
- [38] P. Rodríguez, J. Ulloa, C. Samaniego, and E. Samaniego. A variational approach to the phase field modeling of brittle and ductile fracture. *International Journal of Mechanical Sciences*, 144:502–517, 2018.
- [39] J. Fang, C. Wu, J. Li, Q. Liu, C. Wu, G. Sun, and L. Qing. Phase field fracture in elasto–plastic solids: variational formulation for multi-surface plasticity and effects of plastic yield surfaces and hardening. *International Journal of Mechanical Sciences*, 156:382–396, 2019.
- [40] R. Alessi, M. Ambati, T. Gerasimov, S. Vidoli, and L. De Lorenzis. Comparison of phase-field models of fracture coupled with plasticity. In *Advances in Computational Plasticity*, pages 1–21. Springer, 2018.
- [41] B. Yin and M. Kaliske. A ductile phase-field model based on degrading the fracture toughness: Theory and implementation at small strain. *Computer Methods in Applied Mechanics and Engineering*, 366:113068, 2020.
- [42] A. Mesgarnejad, A. Imanian, and A. Karma. Phase-field models for fatigue crack growth. *Theoretical and Applied Fracture Mechanics*, 103:102282, 2019.
- [43] M. Seiler, T. Linse, P. Hantschke, and M. Kästner. An efficient phase-field model for fatigue fracture in ductile materials. *Engineering Fracture Mechanics*, 224:106807, 2020.
- [44] Y.S. Lo, M.J. Borden, K. Ravi-Chandar, and C.M. Landis. A phase-field model for fatigue crack growth. *Journal of the Mechanics and Physics of Solids*, 132:103684, 2019.

- [45] G.A. Haveroth, M.G. Vale, M.L. Bittencourt, and J.L. Boldrini. A non-isothermal thermodynamically consistent phase field model for damage, fracture and fatigue evolutions in elasto-plastic materials. *Computer Methods in Applied Mechanics and Engineering*, 364:112962, 2020.
- [46] C. Schreiber, C. Kuhn, R. Müller, and T. Zohdi. A phase field modeling approach of cyclic fatigue crack growth. *International Journal of Fracture*, 225(1):89–100, 2020.
- [47] P.J. Loew, B. Peters, and L.A.A. Beex. Fatigue phase-field damage modeling of rubber using viscous dissipation: Crack nucleation and propagation. *Mechanics of Materials*, 142:103282, 2020.
- [48] P.J. Loew, L.H. Poh, B. Peters, and L.A.A. Beex. Accelerating fatigue simulations of a phase-field damage model for rubber. *Computer Methods in Applied Mechanics and Engineering*, 370:113247, 2020.
- [49] J.L. Chaboche. Time-independent constitutive theories for cyclic plasticity. *International Journal of Plasticity*, 2(2):149–188, 1986.
- [50] J.L. Chaboche. Constitutive equations for cyclic plasticity and cyclic viscoplasticity. *International Journal of Plasticity*, 5(3):247–302, 1989.
- [51] J.L. Chaboche. On some modifications of kinematic hardening to improve the description of ratchetting effects. *International Journal of Plasticity*, 7(7):661–678, 1991.
- [52] G.T. Houlsby, C.N. Abadie, W.J.A.P. Beuckelaers, and B.W. Byrne. A model for nonlinear hysteretic and ratcheting behaviour. *International Journal of Solids and Structures*, 120:67–80, 2017.
- [53] P.J. Armstrong and C.O. Frederick. A mathematical representation of the multiaxial baushinger effect. Technical Report RD/B/N 731, Berkeley Nuclear Laboratories, Central Electricity Generating Board, 1966.
- [54] C.O. Frederick and P.J. Armstrong. A mathematical representation of the multiaxial baushinger effect. *Materials at High Temperatures*, 24(1):1–26, 2007.
- [55] J.J. Moreau. Sur les lois de frottement, de viscosité et de plasticité. *Comptes rendus de l'Académie des Sciences, Paris*, 271:608–611, 1970.
- [56] B. Halphen and Q.S. Nguyen. Generalized standard materials. *Journal de Mécanique*, 14(1):39–63, 1975.
- [57] P. Germain, P. Suquet, and Q.S. Nguyen. Continuum thermodynamics. *Journal of Applied Mechanics*, 50:1010–1020, 1983.
- [58] H. Ziegler and C. Wehrli. The derivation of constitutive relations from the free energy and the dissipation function. In *Advances in Applied Mechanics*, volume 25, pages 183–238. Elsevier, 1987.
- [59] J.C. Simo, J.G. Kennedy, and R.L. Taylor. Complementary mixed finite element formulations for elastoplasticity. *Computer Methods in Applied Mechanics and Engineering*, 74(2):177–206, 1989.
- [60] C. Comi and U. Perego. A unified approach for variationally consistent finite elements in elastoplasticity. *Computer Methods in Applied Mechanics and Engineering*, 121(1-4):323–344, 1995.

- [61] W. Han and B.D. Reddy. *Plasticity: mathematical theory and numerical analysis*, volume 9. Springer Science & Business Media, 1999.
- [62] K. Hackl. Generalized standard media and variational principles in classical and finite strain elastoplasticity. *Journal of the Mechanics and Physics of Solids*, 45(5):667–688, 1997.
- [63] M. Ortiz and L. Stainier. The variational formulation of viscoplastic constitutive updates. *Computer Methods in Applied Mechanics and Engineering*, 171(3-4):419–444, 1999.
- [64] C. Miehe. Strain-driven homogenization of inelastic microstructures and composites based on an incremental variational formulation. *International Journal for Numerical Methods in Engineering*, 55(11):1285–1322, 2002.
- [65] C. Carstensen, K. Hackl, and A. Mielke. Non-convex potentials and microstructures in finite-strain plasticity. In *Proceedings of the Royal Society of London A: Mathematical, Physical and Engineering Sciences*, volume 458, pages 299–317. The Royal Society, 2002.
- [66] C. Comi. Computational modelling of gradient-enhanced damage in quasi-brittle materials. *Mechanics of Cohesive-frictional Materials*, 4(1):17–36, 1999.
- [67] M.E. Gurtin and L. Anand. Thermodynamics applied to gradient theories involving the accumulated plastic strain: the theories of Aifantis and Fleck and Hutchinson and their generalization. *Journal of the Mechanics and Physics of Solids*, 57(3):405–421, 2009.
- [68] N.A. Fleck and J.R. Willis. A mathematical basis for strain-gradient plasticity theory—part I: Scalar plastic multiplier. *Journal of the Mechanics and Physics of Solids*, 57(1):161–177, 2009.
- [69] G.A. Maugin. The method of virtual power in continuum mechanics: Application to coupled fields. *Acta Mechanica*, 35(1-2):1–70, 1980.
- [70] H. Petryk. Incremental energy minimization in dissipative solids. *Comptes Rendus Mecanique*, 331(7):469–474, 2003.
- [71] A. Mielke. A mathematical framework for generalized standard materials in the rate-independent case. *Multifield Problems in Solid and Fluid Mechanics*, 28:399–428, 2006.
- [72] A. Mielke and T. Roubíček. *Rate-Independent systems. Theory and application*. Springer, 2015.
- [73] R. Alessi. Energetic formulation for rate-independent processes: remarks on discontinuous evolutions with a simple example. *Acta Mechanica*, 227(10):2805–2829, 2016.
- [74] G. Lancioni. Modeling the response of tensile steel bars by means of incremental energy minimization. *Journal of Elasticity*, 121(1):25–54, 2015.
- [75] O. Rokoš, J. Zeman, and M. Jirásek. Localization analysis of an energy-based fourth-order gradient plasticity model. *European Journal of Mechanics-A/Solids*, 55:256–277, 2016.

- [76] M. Luege, A. Orlando, M.E. Almenar, and E.A. Pilotta. An energetic formulation of a gradient damage model for concrete and its numerical implementation. *International Journal of Solids and Structures*, 155:160–184, 2018.
- [77] R. Alessi, J.J. Marigo, and S. Vidoli. Gradient damage models coupled with plasticity and nucleation of cohesive cracks. *Archive for Rational Mechanics and Analysis*, 214(2):575–615, 2014.
- [78] R. Alessi and D. Bernardini. Analysis of localization phenomena in shape memory alloys bars by a variational approach. *International Journal of Solids and Structures*, 73:113–133, 2015.
- [79] R. Alessi and K. Pham. Variational formulation and stability analysis of a three dimensional superelastic model for shape memory alloys. *Journal of the Mechanics and Physics of Solids*, 87:150–176, 2016.
- [80] J. Mosler and O.T. Bruhns. Towards variational constitutive updates for non-associative plasticity models at finite strain: models based on a volumetric-deviatoric split. *International Journal of Solids and Structures*, 46(7-8):1676–1684, 2009.
- [81] J. Mosler. Variationally consistent modeling of finite strain plasticity theory with non-linear kinematic hardening. *Computer Methods in Applied Mechanics and Engineering*, 199(45-48):2753–2764, 2010.
- [82] G.A. Francfort and U. Stefanelli. Quasi-static evolution for the Armstrong–Frederick hardening-plasticity model. *Applied Mathematics Research eXpress*, 2013(2):297–344, 2013.
- [83] G.A. Francfort. Recovering convexity in non-associated plasticity. *Comptes Rendus Mécanique*, 346(3):198–205, 2018.
- [84] R. Alessi, V. Crismale, and G. Orlando. Fatigue effects in elastic materials with variational damage models: A vanishing viscosity approach. *Journal of Nonlinear Science*, 29(3):1041–1094, 2019.
- [85] G.T. Houlsby and A.M. Puzrin. *Principles of hyperplasticity: an approach to plasticity theory based on thermodynamic principles*. Springer Science & Business Media, 2007.
- [86] M.A. Biot. *Mechanics of incremental deformations*. Wiley, 1965.
- [87] A. Mielke and R. Rossi. Existence and uniqueness results for a class of rate-independent hysteresis problems. *Mathematical Models and Methods in Applied Sciences*, 17(01):81–123, 2007.
- [88] L. Stainier. Consistent incremental approximation of dissipation pseudo-potentials in the variational formulation of thermo-mechanical constitutive updates. *Mechanics Research Communications*, 38(4):315–319, 2011.
- [89] L. Brassart, L. Stainier, I. Doghri, and L. Delannay. Homogenization of elasto-(visco) plastic composites based on an incremental variational principle. *International Journal of Plasticity*, 36:86–112, 2012.
- [90] E. Tanne. *Variational phase-field models from brittle to ductile fracture: nucleation and propagation*. PhD thesis, Université Paris-Saclay (ComUE), 2017.
- [91] E. Samaniego, J. Ulloa, P. Rodríguez, and C. Samaniego. Variational modelling of strain localization in solids: a computational mechanics point of view. *Archives of Computational Methods in Engineering*, pages 1–21, 2020.

- [92] C.N. Abadie. *Cyclic lateral loading of monopile foundations in cohesionless soils*. PhD thesis, 2015.
- [93] H.B. Mühlhaus and E.C. Alfantis. A variational principle for gradient plasticity. *International Journal of Solids and Structures*, 28(7):845–857, 1991.
- [94] R. de Borst and H.B. Mühlhaus. Gradient-dependent plasticity: formulation and algorithmic aspects. *International Journal for Numerical Methods in Engineering*, 35:521–539, 1992.
- [95] Q.S. Nguyen. Quasi-static responses and variational principles in gradient plasticity. *Journal of the Mechanics and Physics of Solids*, 97:156–167, 2016.
- [96] G.A. Maugin. *The thermomechanics of plasticity and fracture*, volume 7. Cambridge University Press, 1992.
- [97] J.C. Simo and T.J.R. Hughes. *Computational inelasticity*. Springer, 1998.
- [98] C. Miehe, S. Teichtmeister, and F. Aldakheel. Phase-field modelling of ductile fracture: a variational gradient-extended plasticity-damage theory and its micromorphic regularization. *Philosophical Transactions of the Royal Society A: Mathematical, Physical and Engineering Science*, 374(2066):20150170, 2016.
- [99] H. Amor, J.J. Marigo, and C. Maurini. Regularized formulation of the variational brittle fracture with unilateral contact: numerical experiments. *Journal of the Mechanics and Physics of Solids*, 57(8):1209–1229, 2009.
- [100] L. Ambrosio and V.M. Tortorelli. Approximation of functional depending on jumps by elliptic functional via Γ -convergence. *Communications on Pure and Applied Mathematics*, 43(8):999–1036, 1990.
- [101] B. Bourdin. Numerical implementation of the variational formulation for quasi-static brittle fracture. *Interfaces and Free Boundaries*, 9(3):411–430, 2007.
- [102] T. Gerasimov and L. De Lorenzis. On penalization in variational phase-field models of brittle fracture. *Computer Methods in Applied Mechanics and Engineering*, 354(2):990–1026, 2019.
- [103] G. Lancioni and G. Royer-Carfagni. The variational approach to fracture mechanics. a practical application to the french panthéon in paris. *Journal of Elasticity*, 95(1-2):1–30, 2009.
- [104] F. Freddi. Fracture energy in phase field models. *Mechanics Research Communications*, 96:29–36, 2019.
- [105] A.S.J. Suiker and R. de Borst. A numerical model for the cyclic deterioration of railway tracks. *International Journal for Numerical Methods in Engineering*, 57(4):441–470, 2003.
- [106] A. Niemunis, T. Wichtmann, and T. Triantafyllidis. A high-cycle accumulation model for sand. *Computers and Geotechnics*, 32(4):245–263, 2005.
- [107] S. François, C. Karg, W. Haegeman, and G. Degrande. A numerical model for foundation settlements due to deformation accumulation in granular soils under repeated small amplitude dynamic loading. *International Journal for Numerical and Analytical Methods in Geomechanics*, 34(3):273–296, 2010.
- [108] L. Brassart, K. Zhao, and Z. Suo. Cyclic plasticity and shakedown in high-capacity electrodes of lithium-ion batteries. *International Journal of Solids and Structures*, 50(7-8):1120–1129, 2013.

- [109] M. Peigney. Cyclic steady states in diffusion-induced plasticity with applications to lithium-ion batteries. *Journal of the Mechanics and Physics of Solids*, 111:530–556, 2018.
- [110] C. Martin and W. Sun. Fatigue damage of collagenous tissues: experiment, modeling and simulation studies. *Journal of Long-Term Effects of Medical Implants*, 25(1-2), 2015.
- [111] H. Dong, M. Liu, C. Martin, and W. Sun. A residual stiffness-based model for the fatigue damage of biological soft tissues. *Journal of the Mechanics and Physics of Solids*, 143:104074, 2020.
- [112] L. Preziosi, D. Ambrosi, and C. Verdier. An elasto-visco-plastic model of cell aggregates. *Journal of Theoretical Biology*, 262(1):35–47, 2010.
- [113] L. Preziosi and G. Vitale. A multiphase model of tumor and tissue growth including cell adhesion and plastic reorganization. *Mathematical Models and Methods in Applied Sciences*, 21(09):1901–1932, 2011.
- [114] G. Sciumè, W.G. Gray, M. Ferrari, P. Decuzzi, and B.A. Schrefler. On computational modeling in tumor growth. *Archives of Computational Methods in Engineering*, 20(4):327–352, 2013.